

# ISP-AD: A Large-Scale Real-World Dataset for Advancing Industrial Anomaly Detection with Synthetic and Real Defects

Paul Josef Krassnig<sup>1,2\*</sup> and Dieter Paul Gruber<sup>1,2</sup>

<sup>1</sup>Polymer Competence Center Leoben GmbH, Leoben, Austria.

<sup>2</sup>Chair of Materials Science and Testing of Polymers, Montanuniversität Leoben, Leoben, Austria.

\*Corresponding author(s). E-mail(s): [paul.krassnig@pccl.at](mailto:paul.krassnig@pccl.at);

[paul-josef.krassnig@stud.unileoben.ac.at](mailto:paul-josef.krassnig@stud.unileoben.ac.at);

Contributing authors: [dieter.gruber@pccl.at](mailto:dieter.gruber@pccl.at);

## Abstract

Automatic visual inspection using machine learning plays a key role in achieving zero-defect policies in industry. Research on anomaly detection is constrained by the availability of datasets that capture complex defect appearances and imperfect imaging conditions, which are typical of production processes. Recent benchmarks indicate that most publicly available datasets are biased towards optimal imaging conditions, leading to an overestimation of their applicability in real-world industrial scenarios. To address this gap, we introduce the Industrial Screen Printing Anomaly Detection Dataset (ISP-AD). It presents challenging small and weakly contrasted surface defects embedded within structured patterns exhibiting high permitted design variability. To the best of our knowledge, it is the largest publicly available industrial dataset to date, including both synthetic and real defects collected directly from the factory floor. Beyond benchmarking recent unsupervised anomaly detection methods, experiments on a mixed supervised training strategy, incorporating both synthesized and real defects, were conducted. Experiments show that even a small amount of injected, weakly labeled real defects improves generalization. Furthermore, starting from training on purely synthetic defects, emerging real defective samples can be efficiently integrated into subsequent scalable training. Overall, our findings indicate that model-free synthetic defects can provide a cold-start baseline, whereas a small number of injected real defects refine the decision boundary for previously unseen defect characteristics, thereby meeting key industrial inspection requirements such as low false positive rates and high recall. The presented unsupervised and supervised dataset splits are designed to emphasize research on unsupervised, self-supervised, and supervised approaches, enhancing their applicability to industrial settings.

**Keywords:** Industrial Anomaly Detection, Industrial Anomaly Detection Dataset, Surface Defect Detection, Synthetic Defects, Automatic Visual Inspection

## 1 Introduction

With the affordability of modern computing power, the research and subsequent application

of deep learning-based surface defect detection in industry is on the rise [Jha and Babiceanu \(2023\)](#); [Prunella et al. \(2023\)](#). As part of smart manufacturing and emerging Industry 5.0, recent

publications address surface defect detection as an anomaly detection problem [J. Liu et al. \(2024\)](#); [Lohweg \(2023\)](#); [Wen, Zhang, Hu, and Li \(2024\)](#). In the context of surface defect inspection, an anomaly can be defined as any unwanted deviation from the sample's permitted surface variability and appearance, which could have known and unknown characteristics. Furthermore, the rare occurrence of anomalies compared to fault-free instances leads to heavily imbalanced data distributions [Bai et al. \(2024\)](#). These anomalies can affect both the aesthetic and functional properties of the product and are therefore of major interest to industrial quality control. Up to now manual inspection by humans is still part of industrial quality control. This repetitive task is prone to subjective assessment and fatigue resulting in quality fluctuations [Chin and Harlow \(1982\)](#); [Kujawińska and Vogt \(2015\)](#). Integrating automated visual inspection processes into the factory floor enables improved product quality, efficiency by reducing human labor, their subjective assessment as well as subsequent production costs. Furthermore, its application is not limited to specific industries and is already used in the e.g. automotive, textile, electronics and agriculture industries [Raisul Islam et al. \(2024\)](#).

A key element of any machine vision system is its underlying defect detection algorithm, enabling the decision-making process of categorizing a sample as fault-free (normal) or defective (anomalous) [Ren, Fang, Yan, and Wu \(2022\)](#). The performance of machine-learning and more specific deep learning-based methods is dependent on the quality and amount of available data. Supervised algorithms based on deep convolutional neural networks (DCNN) [LeCun, Bengio, and Hinton \(2015\)](#) have gained remarkable performance in various defect detection tasks, relying on large labeled datasets [Saberi-Ronaghi, Ren, and El-Gindy \(2023\)](#); [Zheng, Zheng, Kong, and Chen \(2021\)](#).

However, collecting large amounts of fault-free and defective data and subsequent labeling is labor-intensive and often impractical in many industrial scenarios. Additionally, supervised methods struggle to generalize to unseen defects that were not part of the training data. To address these issues, current research focuses on unsupervised anomaly detection methods [Cui,](#)

[Liu, and Lian \(2023\)](#). These methods solely rely on fault-free samples during training, learning feature representations of its underlying normal data distribution. With the publication of datasets such as MVTec [Bergmann, Batzner, Fäuser, Sattlegger, and Steger \(2021\)](#), a wide range of different approaches have emerged, usually based on the comparison of image features or the reconstruction of normal image instances.

Extracted features, obtained by means of layers of e.g. DCNN, are applied in memory bank [Lee, Lee, and Song \(2022\)](#); [Roth et al. \(2022\)](#); [Xie, Wang, Liu, Zheng, and Jin \(2023\)](#), normalizing flow [Tailanian, Pardo, and Musé \(2024\)](#); [Yu et al. \(2021\)](#); [Zhou, Xu, Song, Shen, and Shen \(2024\)](#) or knowledge distillation-based approaches [Batzner, Heckler, and König \(2024\)](#); [Bergmann, Fäuser, Sattlegger, and Steger \(2020\)](#); [Rudolph, Wehrbein, Rosenhahn, and Wandt \(2023\)](#). During inference, extracted test features are compared to learned normal representations using distance metrics or distribution mappings.

Reconstruction-based methods using autoencoders [Bergmann, Löwe, Fäuser, Sattlegger, and Steger \(2019\)](#) or generative adversarial networks (GAN) [L. Zhang, Dai, Fan, and He \(2022\)](#) attempt to reconstruct normal image regions while failing in resembling anomalies, resulting in anomaly scores.

These approaches suffer from poor reconstruction performance on fine-grained structures as well as demanding model training (mode collapse in GANs). Recently, diffusion-based approaches [Mousakhani, Brox, and Tayyub \(2023\)](#); [Tebbe and Tayyub \(2024\)](#); [H. Zhang, Wang, Wu, and Jiang \(2023\)](#) have gained increased attention, to address reconstruction limitations. These methods utilize iterative noising and denoising processes to model underlying data distributions at a computationally intensive cost.

Additional approaches are based on the synthetization of defects in both image and/or feature spaces, showing improved detection performance on image and pixel-level tasks [J. Liu et al. \(2024\)](#); [Zavrtanik, Kristan, and Skočaj \(2022\)](#).

Due to the inherent nature of manufacturing processes, defective samples accumulate over time. Despite the promising detection performance of unsupervised methods, their ability to utilize defective data is limited. Consequently, incorporating both real and synthesized defects

into the training process is emerging as a viable strategy, enhancing the method’s discriminative capabilities.

In addition to defect detection performance, the industrial applicability of a defect detection method depends on meeting process requirements such as process cycle times, adaptability to different products, and robustness to permitted design variability and varying operational conditions. To evaluate model performance in an industrial setting, a dataset that reflects these conditions is crucial. However, a review of the literature shows that most publicly available datasets are generated under “laboratory conditions”, failing to capture the complexities of industrial environments [Alzarooni et al. \(2025\)](#); [J. Liu et al. \(2024\)](#). As a result, the benchmarks of state-of-the-art (SOTA) anomaly detection methods on these datasets are often overestimated compared to real-world industrial scenarios.

## 1.1 Contributions

The aim of this publication is twofold. First, to bridge the gap to industry, we introduce the Industrial Screen Printing Anomaly Detection Dataset (ISP-AD), derived from a real-world industrial use case in screen printing. This dataset provides both unsupervised and supervised training data, comprising synthetic and real defects collected during production. Second, we investigate a mixed supervised training strategy that efficiently utilizes available weakly labeled data consisting of both synthetic and real defects.

We envision the ISP-AD dataset as a research and development resource for advancing anomaly detection methods under realistic industrial conditions. Furthermore, we hope that it will contribute to a more application-oriented perspective, by helping to define paradigms and approaches that align with real-world requirements.

Thus, the main contributions of this work can be summarized as follows:

- **Introduction of the Industrial Screen Printing Anomaly Detection Dataset (ISP-AD) :** a novel large-scale dataset of structured patterns captured using three different optical modalities. The dataset originates from a real-world industrial screen printing process

and includes permitted process-specific variability. With a total of 312 674 fault-free samples and 246 375 defective samples (of which 245 664 are synthetic and 711 are real), it represents the largest publicly available industrial defect detection dataset to date, enabling both unsupervised and supervised training scenarios ([Data availability](#)).

- **Benchmarking of SOTA unsupervised methods:** comprehensive image- and pixel-level evaluations on ISP-AD highlight the challenges posed by small and weakly contrasted defects embedded within high permitted design variability, establishing ISP-AD as a demanding benchmark under industrial conditions.
- **Extended experimental investigation and formalization of mixed supervised training:** building on our earlier work on mixed training [Haselmann M. , Krassnig, P. J., and Gruber D. P. \(2022\)](#), we analyze the incremental incorporation of weakly labeled real defects into synthetic cold-start training across multiple modalities and defect fractions. We formalize the strategy as a *stochastic batch-level injection scheme*, where real defects replace patches in a balanced synthetic stream with an injection probability  $p_{\text{inj}} \in [1/B, 0.25]$ . This condition ensures that real defects complement rather than dominate the synthetic stream, providing controllable stochasticity. Experiments show that even small amounts of previously unseen defects can substantially enhance generalization, efficiently complementing synthetic training data.
- **Methodological insights into adaptive and scalable training strategies:** the mixed supervised training is proposed as an adaptive closed-set strategy operating under a restricted open-set paradigm, where synthetic defects define an initial decision boundary and real defects are incorporated in subsequent retraining stages for iterative refinement within the known process domain. Ablations across ResNet [K. He, Zhang, Ren, and Sun \(2016\)](#), EfficientNet [Tan and Le \(2019\)](#), and ConvNeXt [Z. Liu et al. \(2022\)](#) backbones confirm the architecture-agnostic scalability of the approach, demonstrating robustness under different accuracy–efficiency trade-offs and suitability for industrial deployment.

The structure of the research work is as follows: Section 2 gives an overview of emerging industrial anomaly detection methods as well as available datasets, and highlights existing research gaps. Section 3 introduces the real-world ISP-AD dataset, including the dataset generation process, available data splits, and its limitations. Section 4 describes the applied defect detection methods, the proposed mixed supervised training, and the investigated SOTA unsupervised methods. Section 5 presents the benchmark results across all three optical modalities. Finally, section 6 concludes the work and outlines future research directions.

## 2 State of the Art

### 2.1 Supervision in Industrial Anomaly Detection

Unsupervised methods do not rely on defective samples during training, avoiding the risk of bias towards seen anomalies that can occur in supervised settings. However, the absence of knowledge about anomalous data results in a lack of discriminative features, making it challenging to distinguish subtle anomalies from normal data Ding, Pang, and Shen (2022); Yao, Li, Zhang, Sun, and Zhang (2023). This can result in false positives for normal samples with high permitted variability or overlooked defective areas.

To address this, augmentation methods have emerged that synthesize defective samples, enabling models to learn more discriminative features by incorporating these synthetic representations during self-supervised training tasks. Methods like CutPaste or NSA Li, Sohn, Yoon, and Pfister (2021); Schlüter, Tan, Hou, and Kainz (2022) synthesize defective samples by cropping patches from normal samples, augmenting them (e.g., resizing or rotating), and either pasting them or blending them into random positions using techniques like Poisson image editing Pérez, Gangnet, and Blake (2023).

In contrast to sampling from the examined data distribution, DRAEM Zavrtanik, Kristan, and Skočaj (2021) generates diverse defect shapes by extracting textures from different domains (out-of-distribution) Cimpoi, Maji, Kokkinos, Mohamed, and Vedaldi (2014) using masks generated via Perlin noise Perlin (1985). Additional

approaches use gaussian or simplex noise Perlin (2002) added onto normal images to generate synthetic anomalies Cao, Xu, Liu, and Shen (2023); Tien et al. (2023). More realistic defects, referred to as in-distribution defects, can be achieved by generating defect textures on normal samples by means of random walks Haselmann and Gruber (2017).

Recent trends leverage generative models such as GANs and diffusion-based approaches for defect synthetization Duan, Hong, Niu, and Zhang (2023); Gui, Gao, Liu, Wang, and Wu (2025); X. He, Luo, Li, Chen, and Li (2023); Hu et al. (2024); Zhong et al. (2023) GAN-based approaches rely on sufficient training data, including defective samples, and often struggle to synthesize fine grained patterns.

In contrast, denoising diffusion models aim to address these issues by creating more realistic defects while requiring fewer defective samples.

Besides defect synthetization in the image domain, recent methods have shown promising results in generating defects directly in the feature space, e.g., by introducing gaussian noise Z. Liu, Zhou, Xu, and Wang (2023) or sampling from a set of codebook features Zavrtanik et al. (2022). Global and Local Anomaly co-Synthesis Strategy (GLASS) Chen, Luo, Lv, and Zhang (2025) combines constrained defect synthetization at both feature and image levels, resulting in "near-in" and "far-from" normal sample distribution anomalies, achieving SOTA performance on MVTec Bergmann et al. (2021).

However, common problems of image-level synthetization are the lack of realism and diversity, while feature-level synthetization is hard to control but more efficient. As a consequence, additionally leveraging real defective samples accumulated during production is a complementary approach to increase feature diversity.

Research using both synthetic and real samples during training has been reported in binary classification and object detection Dey, De Ridder, Blanco, Halder, and Van Waeyenberge (2024); Haselmann M. , Krassnig, P. J., and Gruber D. P. (2022); Pierre Gutierrez et al. (2021); Posilović, Medak, Subasic, Budimir, and Loncaric (2021) as well as in recent supervised anomaly detection approaches Ding et al. (2022); Rolih, Fučka, and

[Skočaj \(2025\)](#); [H. Zhang, Wu, Wang, Chen, and Jiang \(2023\)](#).

For instance, [Posilović et al. \(2021\)](#) generated synthetic defects using a GAN and trained an object detection architecture with both real and synthetic data, achieving a 5 % improvement in average precision compared to using only real defects. Similarly, [Dey et al. \(2024\)](#) reported enhanced defect detection performance on a small-sized dataset by additionally incorporating synthesized defects generated via a denoising diffusion approach. [FuseDecode Kozamernik and Bračun \(2025\)](#) proposes a novel autoencoder-based anomaly detection model initially trained on noisy, unlabeled data. The predictions assist in generating weakly labeled datasets, enabling mixed supervision with synthesized and collected real defects, thereby reducing labeling efforts.

Compared to supervised classification approaches, supervised anomaly detection methods reduce bias toward seen real defects by incorporating strategies such as out-of-distribution defect synthesis.

## 2.2 Industrial Anomaly Detection Datasets

In addition to efforts in dataset preparation steps, including image capturing, data cleaning, preprocessing, and labeling, obstacles such as compliance standards for the investigated product impede dataset publication. As a result, many publicly available datasets are generated in laboratory settings, attempting to mimic industrial use cases.

Furthermore, due to the rare occurrence of defective samples, the artificial generation of defects is emphasized. This synthetization can be conducted at the image-level using algorithms (e.g., generative models or 3D rendering [Denninger et al. \(2019\)](#)) or manually on physical samples using appropriate tools.

To mitigate the need for defective samples during training, many industrial datasets are designed for unsupervised settings. In such a setting, defective data is only included in validation and/or test splits, minimizing efforts in defective data preparation.

Table 1 visualizes common industrial anomaly detection datasets. The MVTec dataset [Bergmann et al. \(2021\)](#) has significantly impacted the field

by introducing an unsupervised anomaly detection dataset consisting of 15 industrial categories, grouped into 5 texture and 10 object-based classes. The dataset contains a total of 5354 images, including 1258 defective samples with ground truth masks that enable pixel-level evaluation. Images were mostly captured under highly controlled illumination conditions, and defects were manually generated to produce realistic visual appearances.

The VisA dataset [Zou, Jeong, Pemula, Zhang, and Dabeer \(2022\)](#) extended these efforts by including objects with complex structures, such as printed circuit boards, and multiple instances resulting in a dataset twice the size of MVTec. Considering additional industrial scenarios, Real-IAD [C. Wang et al. \(2024\)](#) introduced a multi-view dataset, covering 30 classes of a variety of materials, such as plastic, wood, ceramics etc. In addition, RAD [Cheng, Cao, Chen, and Shen \(2024\)](#), included uneven illuminations and blurry collections to imitate varying real-world inspection conditions.

Despite advancements in dataset size and increased data variability, the data generation process (including defective samples) was still performed manually, leaving domain gaps compared to factory-floor conditions.

Both DAGM [Matthias Wieler \(2007\)](#) and MIAD [Bao et al. \(2023\)](#) are based on synthetic defect generation. DAGM, published in 2007, contains 10 synthetically generated classes summing up to 14 000 fault-free background textures and 2100 defectives, one for each background texture. In contrast, the more recent MIAD contains 105 000 images of various outdoor industrial maintenance scenarios. MIAD leverages 3D graphics software [Denninger et al. \(2019\)](#) to render realistic 3D scenes with varying surface textures, backgrounds and viewpoints on both fault-free and defective objects.

In contrast to above described industrial datasets, including artificial generated defects, samples collected at industrial production lines are of particular interest. The KolektorSDD2 [Božič, Tabernik, and Skočaj \(2021\)](#) dataset addresses a practical real word example, containing complex textured background structures. Defects in this dataset vary in size and shape, ranging from small scratches to large surface imperfections.

**Table 1** Comparison of SOTA anomaly detection datasets by sample size, defect data availability, and generation method (manual, synthetic, real-world). The proposed dataset, ISP-AD, introduces supervised and unsupervised data splits with synthetic and real defects, collected at the factory floor. In addition, ISP-AD addresses key challenges of industrial inspection that are underrepresented in existing datasets: (i) real-world imperfect imaging conditions and high permitted sample variations; (ii) imbalanced test data splits that reflect realistic inspection scenarios; and (iii) small and weakly contrasted defects on structured patterns relative to large sample areas.

Dataset	#Total	#Good	#Defects	#Defects Train	#Classes	Modality	Defect Generation	
MVTec	5354	4096	1258	0	15	rgb/mono	manually	
VisA	10 821	9621	1200	0	12	rgb	manually	
Real-IAD	151 050	99 721	51 329	0	30	rgb	manually	
RAD	1510	286	1224	0	4	rgb	manually	
DAGM	16 100	14 000	2100	1050	10	mono	synthetic	
MIAD	105 000	87 500	17 500	0	7	rgb	synthetic	
KolektorSDD2	3335	2979	356	246	1	rgb	real-world	
Textile	2150	1814	336	0	6	rgb	real-world	
BTAD	2830	2250	580	0	3	rgb	real-world	
VAD	5000	3000	2000	1000	1	rgb	real-world	
<b>ISP-AD</b>	<b>559 049</b>	<b>312 674</b>	<b>711/245 664</b>		<b>446</b>	<b>3</b>	<b>rgb/mono</b>	<b>real-world/synthetic</b>

Another example is a textile dataset [Thomine and Snoussi \(2024\)](#), further referred to as Textile, that reflects imperfect industrial conditions, such as image blurring and environmental contamination. A further inspection application of three different industrial products, showcasing body and surface defects, is presented within the BTAD dataset [Mishra, Verk, Fornasier, Piciarelli, and Foresti \(2021\)](#).

The recently published VAD dataset [Baitieva, Hurych, Besnier, and Bernard \(2024\)](#) bridges the gap to supervised anomaly detection by additionally introducing 1000 defective training images, thereby extending the unsupervised setting. The investigated piezoelectric element in VAD is prone to structural defects (e.g., cracks or pollutions) as well as to logical defects (e.g. wire or solder position).

### 3 Industrial Screen Printing Anomaly Detection Dataset: ISP-AD

Benchmarks on anomaly detection datasets such as MVTec [Bergmann et al. \(2021\)](#) already show high detection performance above 99 % image-level Area Under the Receiver Operating Characteristic curve (AUROC), indicating less demanding inspection scenarios for SOTA anomaly detection methods.

Therefore, recent efforts in dataset generation focus on mimicking real-world inspection conditions by altering viewpoints, illumination, background, or product placement. However, a review of the literature still reveals a gap in the availability of large-scale datasets (several 10 thousand instances) captured at real-world production lines. Compared to clearly pronounced defect classes in certain object categories [Bergmann et al. \(2021\); Mishra et al. \(2021\); Zou et al. \(2022\)](#), introducing small-scale and subtle defects is important for creating more challenging datasets. Additionally, most datasets are prepared for unsupervised settings, not considering additional defective training samples for supervised approaches.

The proposed industrial dataset aims to address known limitations by introducing the following features:

1. Data captured from a real-world industrial manufacturing scenario.
2. Small and weakly contrasted defects on structured patterns, relative to large sample areas.
3. Three imaging modalities to enhance data variety.
4. Large-scale industrial data splits applicable to both unsupervised and supervised settings. Test splits are imbalanced, typical to manufacturing data distributions (zero-defect policies).
5. Synthetic and collected real defective data accumulated during production, suitable for additional supervision.

6. High permitted sample variations arising from the sample itself, preprocessing, and imperfect imaging conditions.

This section provides a brief overview of the sample under investigation and its defect classes. Additionally, the process of dataset generation, its specifications, and limitations.

### 3.1 Industrial Screen Printing and Defect Classes

The examined product is manufactured using a technique called screen or silk-screen printing [Biegeleisen \(2012\)](#). It is a low-cost and highly automatable manufacturing process applied in various industries e.g. automotive, textile and electronics [Sauer, Meilchen, Kallede, Mennig, and Schmidt \(2011\)](#). In a nutshell, during the printing process, ink is deposited through a stencil with a predefined design onto the front and/or backside of a polymer carrier foil. The subsequent repetition using different stencils and colors results in a multilayer decorated foil plate with a high-quality appealing design. However, the complex manufacturing process is error-prone at basically every step of production. This results in a wide range of different defect appearances and classes. The investigated defect classes within this publication are visualized in Fig. 1 and Fig. 2. They can be divided in punctual defects (Fig. 1), such as inclusions, scratches, dots, pinholes, printing or screen defects or area defects (Fig. 2), such as pattern misalignment, squeegee strokes and grid defects. As described in [Krassnig, P. J., Haselmann M., and Gruber D. P. \(2022\)](#), three different optical modalities, consisting of darkfield illumination in Line Scan Modality 1 (LSM-1), brightfield illumination in Area Scan Modality (ASM), and transmission illumination in Line Scan Modality 2 (LSM-2), were mandatory to visualize the wide range of different defect classes.

For example, most defects in the transparent top layer, such as scratches or mechanical deformations, are only visible under brightfield illumination used in ASM, whereas printing or screen defects are captured under darkfield conditions by means of LSM-1. In LSM-2, transmission illumination is used to detect defects such as pinholes or inhomogeneities within the print layers. For a detailed description of the imaging modalities and a visualization of different defect classes

and their root causes, we refer to sections 2 and 3 in [Krassnig, Haselmann, Kremnitzer, and Gruber \(2024\)](#).

In general, defects can be characterized as small (few px in extension in relation to large sized field of views (FOV) of up to  $10^6 \text{ mm}^2$ , with minimum object pixel sizes of approximately  $75 \text{ }\mu\text{m}$ ) and weakly contrasted. They are embedded within structured background patterns that exhibit high permissible variability, making visual separation difficult due to low contrast, shown by the fiber in Fig. 1. As visualized in Fig. 1 and Fig. 2, defect characteristics are strongly dependent on both the imaging modality and the specific defect class.

### 3.2 Dataset Generation

The generation of appropriate datasets builds the basis for achieving the required defect detection performance of machine learning based methods applied on the production line. Therefore, the design of validation and test splits mimicking the inspection process with its imbalanced data distributions is of utmost importance to perform reliable evaluations. Furthermore, generated data distributions must resemble the imperfect imaging conditions caused by environmental influences (e.g., varying illumination), data processing (varying background, viewpoint and segmentation artifacts), as well as permitted sample variations.

The proposed dataset is based on the work presented in [Krassnig et al. \(2024\)](#), including its efficient data preprocessing and labeling workflow. All samples were collected directly from a real-world screen printing production line at a single industrial site, representing one product design. The investigated product is used in the automotive industry as a decorative element.

Prior to image acquisition, fault-free and defective samples were pre-sorted by domain experts. The sample state is characterized as fixed, thus additional temporal sample alterations can be excluded. Moreover, the samples were selected from different production batches, resembling the permitted design variability. Images were acquired by means of all three optical modalities (LSM-1, LSM-2, ASM) of the inspection system demonstrator installed on the factory floor. The acquired images of fault-free and defective samples were assigned to separate training and test splits. This step avoids any unwanted correlation of fault-free

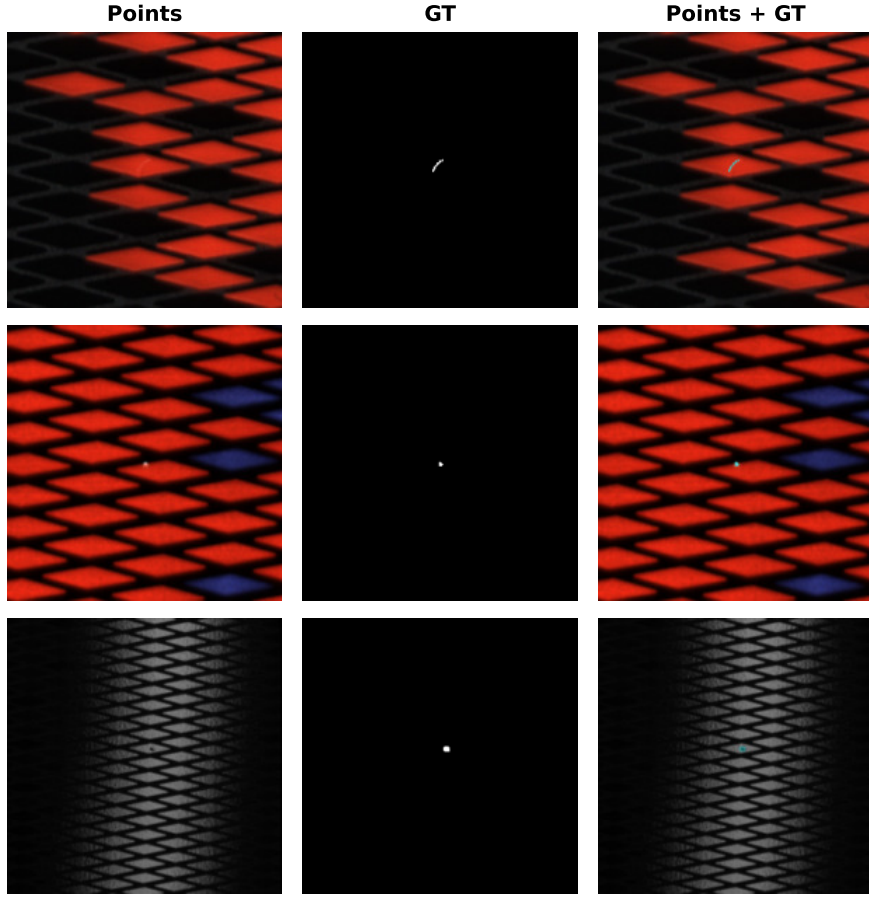


**Fig. 1** Examples of punctual defects from the "Points" defect group, their pixel-level ground truth masks (GT), and overlays (Points + GT). Each row corresponds to a certain defect (fiber, pinhole, mechanical deformation) within its imaging modality (top to bottom: LSM-1, LSM-2, ASM). The pinhole defect in row 2 appears small (few pixels in extension), whereas defects like the fiber in row 1 exhibit low contrast within high sample variability.

and defective patches during the subsequent patch extraction process. A detailed description of the utilized inspection system demonstrator, including its data processing steps, is provided in Section 4 of [Krassnig et al. \(2024\)](#).

The extraction of augmented fault-free training patches (256 x 256 px) at random positions within the region of interest (ROI) is integrated into an automated procedure (steps 1 to 5 in Section 5.1 [Krassnig et al. \(2024\)](#)).

Furthermore, following the central cropping in step 4, synthetic defects according to Section 5.2 are generated in 50 % of the fault-free patches. The utilized algorithm, proposed by [Haselmann and Gruber \(2017\)](#), consists of four steps:

1. Generation of a binary defect skeleton, based on a stochastic process resembling a random walk with momentum.
2. Generation of a random defect texture.
3. Modification of the fault-free patch using the generated texture.
4. Final assessment of defect visibility and rejection of synthesized defects below the visibility threshold.

As described in Section 5.2 in [Krassnig et al. \(2024\)](#), hyperparameters of the random variables were manually adjusted to synthesize bright- and dark-contrasted, punctuate and filamentous morphologies, aiming to imitate real-world defect characteristics, in all three optical modalities (Fig. 3). As a result, balanced supervised training

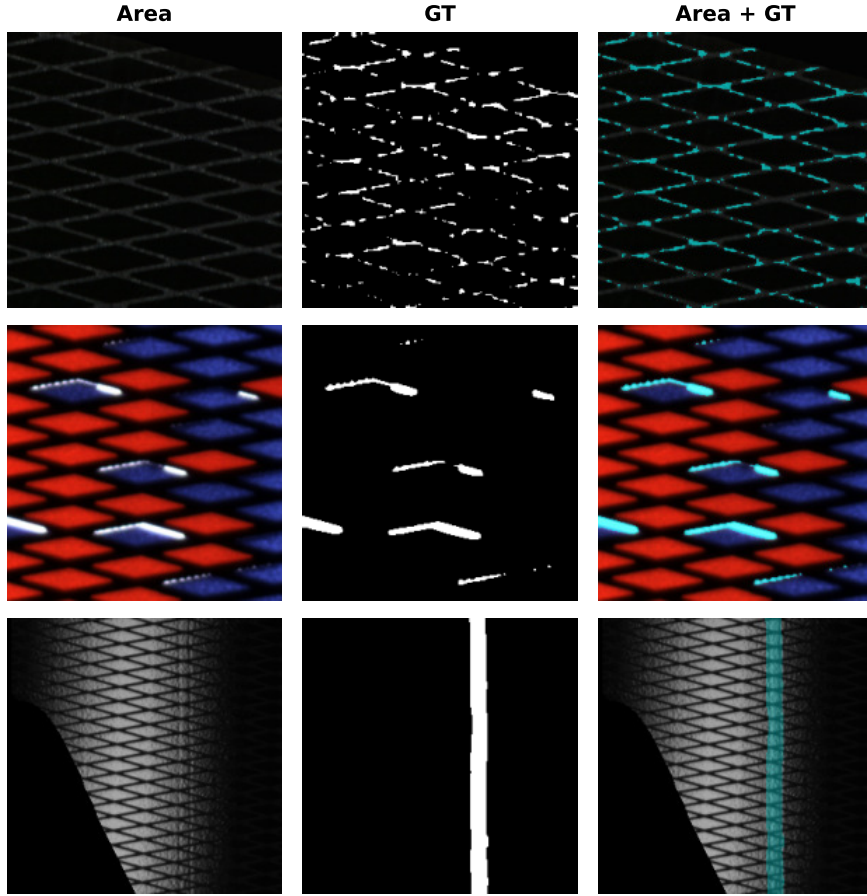


**Fig. 2** Examples of defects from the "Area" defect group, their pixel-level ground truth masks (GT), and overlays (Area + GT). Each row corresponds to a defect (grid, pattern misalignment, squeegee stroke) within its imaging modality (top to bottom: LSM-1, LSM-2, ASM). The pattern misalignment and grid defects exhibit distinct features across the entire patch, while the squeegee stroke appears within the transition area of direct reflection (bottom row).

datasets – also referred to as balanced synthetic streams – were obtained.

Sufficient defect visibility (e.g., via the sum of squared residuals of patch differences as proposed in [Haselmann and Gruber \(2017\)](#)) was determined by manually inspecting up to 100 synthesized defects per data split by a domain expert, and adjusting defect-specific thresholds and hyperparameters accordingly, before applying automatic synthetization to several tens of thousands of patches. Due to compliance regulations, a detailed listing of hyperparameters and their selected values was omitted. However, a full description of the algorithm is available in [Haselmann and Gruber \(2017\)](#).

In addition, real defective patches were manually extracted on selected defective samples in the training and test splits. Thereby, central defect labeling with patch sizes of 512 x 512 px ensures proper defect positioning within augmented patches, which are cropped to a final size of 256 x 256 px during training.

Above described workflow minimizes the manual labeling effort to known defective samples and regions. The underlying image-level labels can be considered "weak" since no ground truth masks are provided, thereby eliminating the need for elaborate pixel-level annotation. In general, patch-based processing is an efficient augmentation technique in upscaling available data, enabling extraction of several 100 000 patches from a few

acquired samples with large FOVs. Theoretically, this automatic patch extraction process is unlimited, although it is restricted by available fault-free samples and FOV sizes [Krassnig et al. \(2024\)](#).

Fault-free test data was generated using a sliding window with a stride of 160 px, extracting overlapping patches (256 x 256 px) to cover a grid. The same patch extraction process was applied to the training data for the unsupervised methods.

As an additional data cleaning step, unwanted defective patches (e.g., contamination in the process environment or defects overlooked by domain experts) were removed from the unsupervised training and general test data.

As described earlier, the automatically extracted fault-free supervised training data was not further screened and can therefore be considered noisy. Based on a manual inspection of 500 randomly extracted and preprocessed (contrast enhanced) patches from LSM-1, it was estimated that 2 - 5 % contained overlooked defects, ranging from borderline cases to clearly contrasted defects such as dust and fibers.

To enable the evaluation of detection performance at the pixel-level, ground truth masks for the test patches were generated using the ilastik labeling tool [Berg et al. \(2019\)](#), which is based on a random forest classifier. Following the assignment of pixel object classes, additional image processing techniques (e.g., erosion and dilation) were applied to ensure distinct defective regions. Examples of selected defective patches, ground truth masks (GT), and their overlays are shown in Fig. 1 and 2.

### 3.2.1 Data Splits

The aim of this publication is to advance research in solving real-world industrial inspection problems by leveraging both synthetic and available real defects accumulated during production processes. Therefore, supervised and unsupervised datasets for each optical modality, acquired from the factory floor, have been created. The supervised training splits include up to approximately 100 000 augmented fault-free patches and 100 000 synthetic defective patches, forming a large-scale balanced synthetic training stream. Additionally, real defective patches, extracted from defective samples representing various defect classes, are categorized into two groups: "area" and "points".

For unsupervised approaches, the fault-free training data includes up to 3678 patches in LSM-1, with reduced splits containing a maximum of 500 patches available for all modalities. These smaller splits are designed to minimize computational effort for e.g. memory demanding methods. The test data for both supervised and unsupervised approaches is identical, mimicking typical imbalanced inspection data distributions. Table 7 summarizes the proposed dataset with its synthetic and real defects available for supervision.

### 3.2.2 Data Format

In general, LSM-1 and LSM-2 patches are provided as 8-bit (rgb) .png files, while ASM patches are provided as single-channel 8-bit .png files. Ground truth masks are stored as single-channel 8-bit .png files. In the case of supervised training data, all patches are stored as single-channel 8-bit within the .hdf5 large file storage format. In addition to the image-level labels, pixel-level GTs are available due to defect synthetization. The folder structure of the unsupervised datasets follows the official MVTec [Bergmann et al. \(2021\)](#) scheme.

### 3.2.3 Augmentation Settings

According to step 3 in Section 5.1 [Krassnig et al. \(2024\)](#), the following augmentation settings were applied to the supervised training data: vertical and horizontal flipping, rotation, shearing, and scaling. Random translation is not included in this list, as it is part of the prior random patch extraction process. Random affine transformations were applied to 80 - 95 % of the extracted patches. In addition, random contrast and brightness adjustments were applied. The corresponding transformation parameters with its values and ranges are shown in Table 8.

### 3.2.4 Additional Data

In addition to proposed data splits, supplementary fault-free patches for all modalities are provided. These patches are the unaugmented counterparts to the fault-free supervised training data described above. They consist of 20 000 and 10 000 fault-free patches in rgb format for LSM-1 and LSM-2, and 20 000 patches in single-channel format for ASM, all stored as .png files.

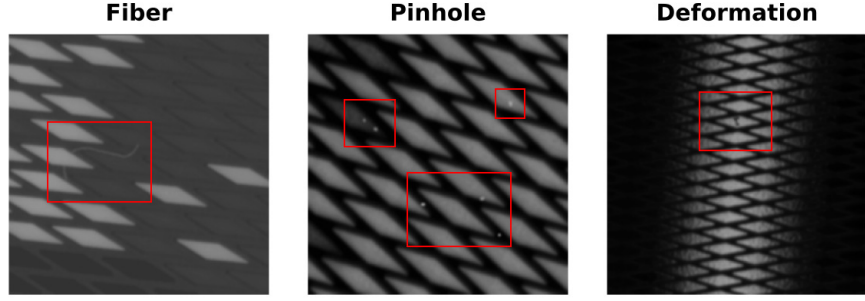


**Fig. 3** Synthesized defects generated using the algorithm proposed in [Haselmann and Gruber \(2017\)](#). Hyperparameters were adjusted to simulate real punctual defects (e.g., pinholes in the middle) and elongated defects (e.g., bright contrasted fiber on the left; small mechanical deformation on the right patch) across all imaging modalities (left to right: LSM-1, LSM-2, ASM).

### 3.2.5 Limitations

Due to the limited amount of defective data available, a validation split was omitted. Although the fault-free patches in the test splits were extensively screened, it cannot be guaranteed that the labels are entirely defect-free.

In ASM, the manual extraction of defective patches introduced additional masked borders on the left and right patch sides (a few pixels in width), which could potentially lead to false positive predictions in non-robust unsupervised approaches, such as reconstruction-based methods. Therefore, cropping these regions during evaluation is recommended to mitigate this effect. Furthermore, the same defects may appear in different patch positions. However, due to varying illumination conditions in this modality, this can be considered an additional form of augmentation.

General limitations include the presentation of a single product design due to compliance regulations, as well as a constrained set of defect classes. However, the observed defect diversity arises from process-related variability and is not strictly limited by the design itself. In addition, ground truth masks for real defective training data are not included, as the focus was set on weakly labeled training data conditions. Although, their inclusion may be considered in future dataset revisions.

## 4 Defect Detection Methods

The recently published work [Krassnig et al. \(2024\)](#) introduced an efficient data preprocessing workflow utilizing weakly labeled defective data in a supervised training approach. Furthermore, the

possible extension to a mixed training strategy using both synthetic and available real defective data [Haselmann M., Krassnig, P. J., and Gruber D. P. \(2022\)](#) was outlined, enhancing defect detection sensitivity of overlooked defect classes.

Therefore, the evaluation of the mixed training strategy on the presented demanding imaging modalities should give further insights in leveraging supervised methods in industrial anomaly detection. For comparison several SOTA unsupervised anomaly detection methods are investigated. Utilized approaches as well as their training settings will be described in the following section.

### 4.1 Mixed Supervised Training

In industrial production, defects emerge at various stages of the manufacturing process and may be unavailable during training or even previously unknown. Thus, defects can be categorized as:

- **Seen defects:** Known defect classes that are available during training (synthetic or real).
- **Unseen defects:** Unknown or unavailable defect classes that may exhibit previously unobserved feature distributions.

The proposed mixed supervised training strategy showed increased detection performance by leveraging both synthetic and real defects during training, compared to training separately on synthetic or real ones [Haselmann M., Krassnig, P. J., and Gruber D. P. \(2022\)](#). Thus, depending on the availability of real defects, the method can be applied in cold-start scenarios, starting with purely synthetic training and transitioning to a

mixed setup as real defects accumulate. This is an important capability in industrial applications, as the model can be improved step by step with newly available defective samples.

However, the ability to synthesize certain defect classes using the algorithm in [Haselmann and Gruber \(2017\)](#), such as squeegee strokes shown in Fig. 2, is limited or even infeasible. Nonetheless, such model-free approaches, as described in [S. Wang et al. \(2025\)](#), do not rely on real defective samples for subsequent model training or conditioning, unlike generative models such as GAN- or diffusion-based methods [Duan et al. \(2023\)](#); [Gui et al. \(2025\)](#); [Hu et al. \(2024\)](#). They may therefore represent a more deployment-friendly strategy, particularly in cold-start scenarios where no real defective samples are available. In other words, model-free anomaly synthetization refers to methods that generate artificial defects through handcrafted, augmentation-based, or procedural rules without training a generative model [Haselmann and Gruber \(2017\)](#); [Li et al. \(2021\)](#); [Schlüter et al. \(2022\)](#); [Zavrtanik et al. \(2021\)](#).

Thus, even small amounts of previously unseen real defects may contribute to learning feature representations that could not be captured by synthetization or were absent in the available real data. Additionally, incorporating real defects, similar to synthesized ones, increases the feature diversity of already seen defects. Throughout this work, we use the term *few-shot* to refer specifically to training or defect modeling regimes with only a limited amount of real defective samples available (e.g., 10 patches), while the majority of training data is still provided by synthetic defective or fault-free patches (see Section 3.2.1 on data splits).

Utilizing the above-introduced datasets, a DCNN pretrained on ImageNet [Jia Deng et al. \(2009\)](#) was trained in a supervised manner. Synthetic defective patches were generated in 50% of the fault-free patches.

During training, each patch in this balanced synthetic stream was replaced by an augmented real defective patch with an injection probability  $p_{\text{inj}}$ , chosen within the range

$$p_{\text{inj}} \in \left[ \frac{1}{B}, 0.25 \right], \quad (1)$$

and kept constant during each training stage, where  $B$  denotes the batch size.

The injection probability  $p_{\text{inj}}$  can be tuned to the quantity and diversity of available real defects: lower values favor specificity, while higher values improve sensitivity but also increase the risk of bias toward injected feature distributions. Therefore, the lower bound ensures that, in expectation, at least one real defect is injected into each batch, while the upper bound of 25% was chosen empirically to prevent real defects from dominating the synthetic stream.

Unlike dataset-level mixing approaches [Dey et al. \(2024\)](#); [Posilović et al. \(2021\)](#) or deterministic batch-level schemes that enforce one real defect per batch [Huang, Zeng, Zhao, Chai, and Yang \(2025\)](#), our method introduces a tunable stochastic injection. This allows adaptation to defect availability and synthesis capabilities while maintaining variability across training batches, ensuring that real defects complement rather than dominate the synthetic stream.

The proposed batch-wise stochastic injection scheme treats each patch independently. Consequently, the expected fraction of real defects in any batch equals  $p_{\text{inj}}$ , regardless of whether the underlying stream consists of purely fault-free patches or of a balanced synthetic-fault-free mixture.

This formulation highlights the connection to our previously published oversampling approach [Krassnig et al. \(2024\)](#): when the balanced synthetic stream is replaced by a pure fault-free stream and the injection probability is set to  $p_{\text{inj}} = 0.5$ , the two approaches converge. In this special case, each batch contains, in expectation, 50% fault-free and 50% real defective patches.

Supervised binary classification is inherently a closed-set problem, in contrast to the open-set problem of anomaly detection described above. In production environments, such as the investigated screen printing process, possible defect causes are often known in advance, even if corresponding defective samples are not yet available. This effectively reduces the defect space to a restricted open-set problem, where not all defects are yet observed, but their characteristics are likely to fall within a range of expected or process-related visual features. To address this setting, our mixed supervised training can be characterized as an adaptable closed-set strategy, operating within

this bounded defect space defined by process-specific visual characteristics, both observed and yet unobserved. Adapting the classifier to emerging, previously unseen defect classes with a minimal set of recently available samples would be an important capability in industrial settings.

The following experiments in Section 5.2 aim to investigate the generalization capabilities of the proposed mixed training strategy for previously unseen defects (e.g., defects that could not be synthesized). In addition, its scalability is examined under varying proportions of collected real defects across all imaging modalities: LSM-1, LSM-2, and ASM. Before the main evaluations, ablation experiments across various backbones were performed.

## 4.2 Training Settings

The network training was performed using the stochastic gradient descent optimizer with the following parameters: a learning rate ranging from  $1 \times 10^{-5}$  to  $5 \times 10^{-4}$ , weight decay of  $1 \times 10^{-2}$ , and momentum of 0.9. Cosine annealing with warm restarts ( $T_0 = 7813$ ,  $T_{mult} = 2$ ) was applied as the learning rate scheduler, following the approach outlined in Loshchilov and Hutter (2016). Based on a backbone ablation experiment comparing ResNet K. He et al. (2016), EfficientNet Tan and Le (2019), and ConvNeXt Z. Liu et al. (2022), ResNet-18 pre-trained on ImageNet Jia Deng et al. (2009) was selected as the backbone, as it provided the best accuracy–efficiency trade-off for the underlying use case (see Section 5.2.1). The final fully connected layer, originally consisting of 1000 output neurons (as per ImageNet pretraining), was replaced by a layer with two output neurons representing the binary class labels ‘good’ and ‘defective’. To mitigate potential domain bias from pretrained weights, all layers of the selected architecture were fine-tuned using the initial learning rate and scheduling scheme described above. As additional regularization, dropout with a rate of 10% was applied to the final fully connected layer of the classifier head.

As part of the preprocessing, patches from LSM-1 were brightness-adjusted by a factor of 1.5. Additionally, weak smoothing was applied across all modalities using a Gaussian kernel with a kernel size of 3 and a sigma of 1. In mixed training scenarios using both synthetic and real defects, the injection probability  $p_{inj}$  for real defects was set to

1/32. Thus, for a batch size of 128, the expected number of augmented real defects per batch was four. This setting aims to prevent overrepresentation of real defects within the balanced synthetic data stream.

Mixed precision training was carried out until the validation loss showed no improvement for 20 consecutive epochs. Model selection was based on the lowest validation loss. As previously described, validation was performed on the available test set. For the binary classification task, thresholds were determined according to the optimal F1-scores obtained.

## 4.3 Unsupervised Methods

In order to compare the defect detection performance to SOTA unsupervised approaches, methods for feature embedding, reconstruction and synthetization are investigated. Thus, the methods used are grouped according to their approaches and thus briefly described. In addition, method and training settings utilized in the experiments are listed.

### 4.3.1 Normalizing Flows

In contrast to utilizing large memory banks for feature comparison, normalizing flows model normal feature distributions. During training, the initial complex normal feature distribution is transformed into a standard normal distribution through a series of invertible mappings. In contrast to DCNNs as feature extractors, U-Flow Tailianian et al. (2024) utilizes a multiscale vision transformer architecture Dosovitskiy (2020), pre-trained independently for each scale. A fully invertible architecture is achieved by adapting a UNet-like structure Ronneberger, Fischer, and Brox (2015) to normalizing flows. Thus, the feature extractor acts as the encoder, while the normalizing flow serves as the decoder.

### 4.3.2 Student-Teacher

Within this approach, a shallow student network attempts to mimic the output of a pre-trained (distilled) teacher using knowledge distillation. Exclusively trained on fault-free data, the distilled student network fails to predict the teacher’s output on anomalous features, resulting in an anomaly score. Efficient-AD Batzner et al. (2024)

provides an lightweight network architecture with restricted receptive field to accelerate feature extraction. Additionally, a hard feature loss function and a loss penalty are introduced to prevent the student from generalizing its imitation to out-of-distribution images. Furthermore an integrated autoencoder ensures detection of logical anomalies.

### 4.3.3 Denoising Diffusion

Denoising diffusion probabilistic models are a class of generative models inspired by non-equilibrium thermodynamics. They consist of a forward diffusion process that gradually adds gaussian noise to the input image over several steps, transforming it into a standard normal distribution. During training, the reverse diffusion process learns to denoise the corrupted image step by step by minimizing the difference (mean squared error) between the predicted noise and the actual noise added during the forward process. The method proposed in Denoising Diffusion Anomaly Detection (DDAD) [Mousakhan et al. \(2023\)](#) utilizes target images to guide the denoising process, improving its ability to reconstruct normal patterns. Anomaly localization is achieved through both feature-wise and pixel-wise comparisons between the reconstructed image and the input image. The pretrained feature extractor is adapted to the target domain using examples generated by the denoising model, further enhancing detection performance.

### 4.3.4 Defect Synthetization

GLASS [Chen et al. \(2025\)](#) extends purely image-level anomaly synthetization by introducing Global Anomaly Synthesis (GAS) at the feature level and Local Anomaly Synthesis (LAS) at the image level. GAS utilizes gaussian noise guided by gradient ascent and truncated projection to synthesize anomalies in the feature space near the normal sample distribution (in-distribution anomalies). LAS generates out-of-distribution anomalies by overlaying textures on normal images using Perlin masks, similar to the approach in [Zavrtanik et al. \(2021\)](#). Finally, a segmentation network is trained end-to-end using three loss functions: normal feature, local anomaly feature, and global anomaly feature loss. During inference, only the normal feature branch is utilized for anomaly detection.

### 4.3.5 Implementation Details

To standardize the evaluation workflow, the Anomalib API [Akcay et al. \(2022\)](#) was utilized for the following unsupervised methods [Batzner et al. \(2024\)](#); [Tailanian et al. \(2024\)](#). Therefore, a training and evaluation pipeline, was implemented. Default method settings, as documented in the model configuration files, were applied. In case of Efficient-AD [Batzner et al. \(2024\)](#), the medium (M) patch descriptor network was chosen.

Additionally, the official implementations of DDAD [Mousakhan et al. \(2023\)](#) and GLASS [Chen et al. \(2025\)](#), along with their configuration files, were selected. The target image conditioning parameters  $w$  and  $w_{DA}$  were set to 3, together with 4 domain adaptation epochs, as specified in DDAD. In GLASS, the manifold hypothesis was selected as the GAS strategy, while foreground masks were omitted in LAS.

In general, the training input shape for image patches was set to 256 x 256 px. Despite center cropping (224 x 224 px) in DDAD for LSM-1, and center cropping (224 x 224 px) in ASM, no additional preprocessing was applied to the raw image patches. Center cropping within ASM excludes any masked borders produced by manual patch extraction (Section 3.2.5). Due to Efficient-AD’s autoencoder architecture, the input shape was kept constant at 256 x 256 px, however during evaluation, border regions were omitted, as shown in Fig. 4. To enable feature extraction by means of the multi-scale vision transformer backbone in U-Flow, patches were resized to 448 x 448 px. Configuration files for all methods are publicly accessible in the dataset repository ([Data availability](#)).

### 4.3.6 Training Settings

Anomalib’s engine was trained until the pixel-level AUROC showed no improvement for 30 consecutive epochs, with a limit of 300 epochs. The denoising diffusion approach was trained for 3000 steps with learning rates ranging from  $5 \times 10^{-5}$  to  $1 \times 10^{-4}$ . During testing, the starting point for the denoising trajectory was set to 250, with a step size of 25. Due to memory limitations, the batch size for both training and testing was reduced to 8. GLASS was trained up to 160 meta-epochs, with learning rates ranging from  $1.25 \times 10^{-5}$  to  $5 \times 10^{-5}$ , also using a batch size of 8. Thresholds

for both image- and pixel-level metrics were determined by computing the optimal F1-score at the image-level. Training was performed on reduced splits of up to 500 patches.

#### 4.3.7 Hardware Setup

Experiments were performed on desktop workstations, equipped with NVIDIA GPUs (GeForce RTX 3090 or GeForce RTX 4080), AMD 16-core processors and 64GB RAM running on OS Windows 10/11. The Python environments (version  $\geq 3.9.15$ ) utilized GPU versions of the PyTorch framework (version  $\geq 2.1.0$ ) with CUDA Toolkit version 11.8, as well as PyTorch Lightning (2.4.0).

## 5 Experiments and Results

The following section investigates the defect detection performance of the supervised and unsupervised approaches proposed in Section 4, applied across all optical modalities: LSM-1, LSM-2, and ASM.

### 5.1 Defect Detection Performance Metrics

In addition to commonly used metrics such as recall, false positive rate (FPR), and AUROC, metrics designed to handle class imbalance effectively were selected. For image-level metrics, the Matthews Correlation Coefficient (MCC) was applied. The MCC, which ranges from -1 (indicating inverse prediction) to 1 (indicating perfect prediction), incorporates all entries of the confusion matrix: true negatives (TN), true positives (TP), false negatives (FN), and false positives (FP). In this context, TN represents correct fault-free predictions, while TP represents correctly predicted defective patches. To account for pixel-level class imbalance, the per region overlap score (PRO) was chosen to assign appropriate weightings to different sized defective regions.

### 5.2 Mixed Supervised Training

To evaluate the scalability of the introduced mixed supervised training, different fractions of real defects accumulated during production were injected into the balanced stream of fault-free and synthetically generated defects. Additionally, to examine adaptability to unseen features, such as

those missed during synthetization, training was performed exclusively on each defect group (points or area).

Following random shuffling of all available defects, fractions of 1/2, 1/4, 1/8, and 1/16 were extracted in an ordered manner. This approach ensures that defects included in smaller fractions are also represented in larger ones. These fractions consist of both defect groups, points (Fig. 1) and area (Fig. 2), representing features that are either punctual or distributed across large sample areas (mixed group). In all experiments, starting from purely synthetic training, real defects were injected with a probability  $p_{\text{inj}}$  of 1/32. To ensure comparability between experiments, the same training settings, including learning rates and seeds, were applied within each optical modality.

Prior to investigating the scalability and generalizability of mixed supervised training, ablation experiments were conducted on LSM-1 to identify an industry-applicable backbone that satisfies process-cycle constraints defined in Krassnig et al. (2024). The results, summarized in Table 2, compare the oversampling approach proposed in Krassnig et al. (2024) with mixed training Haselmann M. , Krassnig, P. J., and Gruber D. P. (2022) across different backbones, defect fractions, and synthetic-only baselines, thereby highlighting accuracy–efficiency trade-offs relevant for industrial inspection. Following the backbone selection, image-level defect detection performance in LSM-1 and ASM across various defect fractions is presented in Tables 3 and 4.

#### 5.2.1 Ablation: Backbone Selection

As defined in Krassnig et al. (2024), the overall inspection time, utilizing all three measurement chambers, was restricted to 15–30 s. To avoid bottlenecks induced by the inference stage, efficient backbones from standard ResNet architectures K. He et al. (2016) as well as more recent EfficientNet and ConvNeXt architectures Z. Liu et al. (2022); Tan and Le (2019) were evaluated.

The inference time measurements reported in Table 2 were determined as the arithmetic mean of five cycles with 100 repetitions, including preprocessing of the respective methods (GeForce RTX 4080 setup as described in Section 4.3.7). Each cycle was preceded by a 10-iteration warm-up.

**Table 2** Ablation study comparing oversampling [Krassnig et al. \(2024\)](#) and mixed training ( $p_{\text{inj}} = 1/32$ ). [Haselmann M.](#), [Krassnig, P. J.](#), and [Gruber D. P. \(2022\)](#) across different backbones (ResNet [K. He et al. \(2016\)](#), EfficientNet [Tan and Le \(2019\)](#), ConvNeXt [Z. Liu et al. \(2022\)](#)), different fractions of real defects, and a synthetic-only baseline on LSM-1. Metrics: MCC, inference time per patch, and throughput (mean  $\pm$  std, patches/s). The best MCC in the **full-data regime** (172 real defects) is highlighted in **bold**, while the best MCC in the **few-shot regime** (10 real defects) is marked with a dagger ( $\dagger$ ).

Model	Strategy	# Real Defects	MCC	Inf. Time (ms)	Throughput (patches/s)
ResNet-18	Oversampling	10	0.70	0.16	$6309 \pm 5$
		172	0.91		
	Mixed	0	0.81		
		10	0.91 $\dagger$		
		172	<b>0.96</b>		
ResNet-50	Oversampling	10	0.78	0.45	$2216 \pm 1$
		172	0.93		
	Mixed	0	0.74		
		10	0.91 $\dagger$		
		172	<b>0.97</b>		
EfficientNet-B0	Oversampling	10	0.73	0.22	$4608 \pm 5$
		172	0.94		
	Mixed	0	0.86		
		10	0.91 $\dagger$		
		172	<b>0.96</b>		
EfficientNet-B4	Oversampling	10	0.74	0.55	$1815 \pm 1$
		172	<b>0.98</b>		
	Mixed	0	0.87		
		10	0.94 $\dagger$		
		172	0.97		
ConvNeXt-Tiny	Oversampling	10	0.80	0.52	$1912 \pm 9$
		172	<b>0.98</b>		
	Mixed	0	0.92		
		10	0.96 $\dagger$		
		172	<b>0.98</b>		

To account for asynchronous CUDA processing, inference times were measured using PyTorch’s synchronized CUDA *events* at a batch size of 128, with *autocast* applied for mixed-precision evaluation.

As shown in Table 2, all architectures achieved fast inference times below 1 ms per patch, although the shallow ResNet-18 outperformed the other backbones by a factor of 1.36 compared to EfficientNet-B0 and up to approximately 3.5 compared to EfficientNet-B4 and ConvNeXt-Tiny.

ConvNeXt-Tiny, a modernized CNN architecture that incorporates depthwise convolutions with larger  $7 \times 7$  kernels together with other design elements inspired by Vision Transformers [Z. Liu et al. \(2022\)](#), achieved the highest MCC values across most training strategies. With all available real defects, pure oversampling achieved a maximum MCC of 0.98. EfficientNet-B4 trained with all available defects also reached an MCC of

0.98. Under these full-data conditions, the mixed training strategy achieved a comparable level of performance.

For all other architectures, mixed training with all available defects yielded higher MCC values, particularly in standard backbones such as ResNet [K. He et al. \(2016\)](#), achieving 0.96 (ResNet-18) and 0.97 (ResNet-50), compared to 0.91 and 0.93 with pure oversampling.

In the few-shot regime (10 real defects), pure oversampling was outperformed by the mixed training strategy by large margins, with MCC improvements of 0.16 (ConvNeXt-Tiny) to 0.21 (ResNet-18). Across all backbones, starting from the purely synthetic baseline, the injection of real defects into the balanced synthetic stream progressively improved defect detection. Even a few injected real defects proved beneficial, achieving MCC values greater than 0.91 across all backbones. Moreover, the ConvNeXt-Tiny architecture

reached a high MCC of 0.96 with just 10 injected real defects, highlighting the superiority of the mixed strategy in few-shot regimes.

Furthermore, the synthetic-only baseline, which did not rely on any real defects for defect generation (model-free approach), outperformed few-shot (10 real defects) oversampling in 4 out of 5 backbone experiments.

Based on the given industrial requirements and to avoid any inference bottleneck, the best accuracy–efficiency trade-off was achieved with the ResNet-18 architecture, reaching performance close to that of more modern architectures when using the mixed training strategy on all available data. Nonetheless, depending on future industrial requirements, ConvNeXt architectures remain a viable choice, delivering industry-applicable detection performance even in the few-shot regime.

### 5.2.2 Scalability and Synthetic Defect Complementation

Based on the ablation, ResNet-18 was selected for the subsequent experiments, as it represented the best accuracy–efficiency trade-off. The scalability of mixed training was evaluated on LSM-1, LSM-2, and ASM. Experiments examined whether small numbers of real defects with previously unseen characteristics—such as squeegee strokes in ASM or grid defects in LSM-1, which could not be synthesized—could complement synthetic features and improve generalization.

Training with purely synthetic defects in LSM-1 resulted in an MCC of 0.81 with an FPR of 0.7 %. As described in the previous publication [Krassnig et al. \(2024\)](#), depending on the underlying preprocessing strategy, FPRs less than 0.59 respectively 0.33 % were necessary to avoid unwanted false alarms, leading to unnecessary sample rejections.

Gradually adding real defective patches increased performance, achieving an MCC of 0.96 when utilizing all 172 available defects. This reduced the number of FN predictions from 22 to 4, representing an 81% reduction. Using only 10 defective patches from both defect groups (mixed) resulted in an MCC of 0.91. For comparison, supervised training with oversampling on all 172 available real defects achieved the same MCC of 0.91 (Table 2).

Training with separated fractions of point and area defects also showed improved detection performance, with area defects having more impact. Adding this defect group reduced group-related FNs from 6 in purely synthetic training to 1 in both mixed training and area-specific fractions. In mixed fractions greater than 1/8, no area defect was overlooked.

Training on the LSM-2 modality achieved near-perfect detection performance, overlooking only a single defective patch. The injection of real defective patches accelerated convergence, requiring only 10 epochs compared to approximately 20 epochs for purely synthetic training. This behavior may be attributed to the clearly pronounced defect characteristics of pinholes and pattern misalignment, as illustrated in Fig. 1 and Fig. 2.

The ASM modality can be defined as the most demanding dataset due to its specific illumination characteristics (see Fig. 2) and imperfect segmentation masks. Training on purely synthetic defects resulted in an MCC of 0.70, which could be significantly improved to greater than 0.95 by utilizing fractions upwards of 1/8. This improvement reduced FNs by up to 93 % through the injection of real defects. The FPRs were comparable to those observed in LSM-1, indicating robustness to permitted sample variations and challenging inspection conditions.

Leveraging the area defect group or mixed fractions had a significantly greater impact on detection performance compared to relying solely on punctual defects. In purely synthetic training, 23 out of 28 FNs were area defects. Training with injected area defects reduced this number to only a few (up to 3). Utilizing all 146 available defects resulted in just 2 FNs, one of each defect group.

Additional experiments using solely real defects within the supervised oversampling approach [Krassnig et al. \(2024\)](#) achieved MCCs greater than 0.98 for fractions upwards of 1/4. The more distinct defect characteristics compared to LSM-1 (e.g. scratches or dots), as well as the limited defect diversity within the test set (see Section 3.2.5), might be reasonable explanations for observed performance saturation.

As observed across other backbones in LSM-1 (Table 2), the performance of the proposed mixed training strategy remained superior in the low data regimes (fractions 1/16 and 1/8), especially when training was performed exclusively on area

**Table 3** Defect detection performance of the investigated mixed supervised training strategy [Haselmann M. , Krassnig, P. J., and Gruber D. P. \(2022\)](#) evaluated on LSM-1. Starting from purely synthetic training, real defective patches were progressively injected with an injection probability  $p_{\text{inj}}$  of 1/32 at varying fractions (1/16, 1/8, 1/4, 1/2, 1) of collected defects. The best-performing fraction, based on image-level MCC, is highlighted in bold.

Defect Group	#Real Defects	MCC	Recall (%)	FPR (%)	TN	TP	FN	FP
-	0	0.81	76.8	0.7	1459	73	22	11
points	10	0.86	82.1	0.5	1463	78	17	7
area	10	0.90	84.2	0.2	1467	80	15	3
mixed	10	0.91	84.2	0.1	1469	80	15	1
mixed	21	0.91	86.3	0.2	1467	82	13	3
mixed	43	0.93	91.6	0.3	1466	87	8	4
mixed	86	0.93	90.5	0.2	1467	86	9	3
mixed	172	<b>0.96</b>	95.8	0.2	1467	91	4	3

**Table 4** Defect detection performance of the investigated mixed supervised training strategy [Haselmann M. , Krassnig, P. J., and Gruber D. P. \(2022\)](#) evaluated on ASM. Starting from purely synthetic training, real defective patches were progressively injected with an injection probability  $p_{\text{inj}}$  of 1/32 at varying fractions (1/16, 1/8, 1/4, 1/2, 1) of collected defects. The best-performing fraction, based on image-level MCC, is highlighted in bold.

Defect Group	#Real Defects	MCC	Recall (%)	FPR (%)	TN	TP	FN	FP
-	0	0.70	62.2	0.6	1905	46	28	11
points	9	0.76	66.2	0.3	1910	49	25	6
area	9	0.91	91.9	0.4	1909	68	6	7
mixed	9	0.94	93.2	0.2	1912	69	5	4
mixed	18	0.92	91.9	0.3	1911	68	6	5
mixed	36	<b>0.97</b>	95.9	0.1	1914	71	3	2
mixed	73	0.96	94.6	0.1	1914	70	4	2
mixed	146	0.96	97.3	0.2	1912	72	2	4

and point defect groups. In these settings, MCCs of 0.91 and 0.76 were achieved, respectively (see Table 4), compared to MCCs of 0.56 and 0.65 for pure oversampling. Furthermore, optimized F1 thresholds below 0.1 indicated majority-class bias in the supervised oversampling strategy in these few-shot regimes.

#### Complementation with Real Defects

As described earlier, the capability to synthesize area defects is limited. In the case of ASM, defect synthetization for the squeegee stroke defect class (Fig. 2) was not possible and can be characterized by having unseen feature distributions. In contrast, LSM-1 contains grid defects (Fig. 2) that exhibit similar punctual features to the synthesized ones. Models trained with synthetic defects generalized better on LSM-1, whereas ASM benefited more strongly from the injection of area defects.

For the ASM modality, the injection of 9 area defects led to an increase in the MCC by 0.21,

reaching 0.91. The injection of similar synthesized feature distributions, as in the case of point defects, proved beneficial for the overall defect detection performance, including previously overlooked punctual defects. Furthermore, training on several tens of thousands of fault-free patches introduced permitted normal feature variability, resulting in industry-applicable FPRs of less than 0.59 respectively 0.33 %.

#### 5.2.3 Key Findings Mixed Training Strategy

Above experiments indicate that mixed training achieves scalable performance across all investigated modalities, with synthetic and real defects complementing each other. (i) In LSM-1, model-free synthetization established a strong initial boundary, achieving an MCC of up to 0.92 in the synthetic-only baseline with ConvNeXt-Tiny. Its capability, however, appeared limited by the synthetization method and the underlying modality: in LSM-1, punctual defect characteristics such

as those occurring in grid defects could be captured to a significant degree synthetically, whereas in ASM, unsynthesizable morphologies such as squeegee strokes required real injection. (ii) Injecting even a few real defects complemented the already learned synthetic features, reducing false negatives and refining the initial boundary. (iii) Mixed training consistently showed superior performance in few-shot regimes, achieving an MCC of at least 0.91 with only 10 real defect samples across various backbones when evaluated on LSM-1. It was beneficial in avoiding majority-class bias, converged faster, and maintained the low FPRs required in industrial inspection. The mixed training strategy proved architecture-agnostic, improving results across ResNet [K. He et al. \(2016\)](#), EfficientNet [Tan and Le \(2019\)](#), and ConvNeXt [Z. Liu et al. \(2022\)](#), with clear trade-offs between detection performance and inference speed.

Together, these findings suggest that synthetic defects can serve as a cold-start baseline, while injected real defects provide complementary information for defect characteristics that cannot be synthesized. Furthermore, these results demonstrate that synthetic data can substantially reduce the number of real samples needed to achieve a given level of detection performance.

Thus, model-free synthesis approaches, as implemented in the proposed algorithm [Haselmann and Gruber \(2017\)](#), which does not require defective training data for elaborate model training, may represent a viable option for rapid deployment in industry, as demonstrated in the proposed industrial use case [Krassnig et al. \(2024\)](#).

#### 5.2.4 Limitations and Future Adaptations

The above results are based on the initial random selection of defective samples and are therefore expected to vary with different seeds during dataset generation. Extensive hyperparameter tuning and statistical analysis are left for future research. In addition, the distribution of available "area" and "points" defect groups is imbalanced, due to limited availability (Table 7).

While this approach avoids the need for a trained generative model, hyperparameter tuning of the defect synthesis algorithm can be elaborate, and the diversity of synthesized defects remains limited.

Depending on data availability and deployment stage, more recent approaches such as generative models or vision language models [Xu et al. \(2025\)](#) could be integrated as synthesis modules within this adaptable closed-set approach. A combination of model-free approaches (e.g. based on Perlin masks [Perlin \(1985\)](#)) with model-based approaches (e.g. diffusion-based models [Gui et al. \(2025\)](#)) could further enhance feature diversity. ISP-AD therefore provides a benchmark, with its additional fault-free data splits enabling the investigation of emerging synthetization methods (see Section 6.1).

### 5.3 Unsupervised Methods

To estimate the defect detection performance of unsupervised methods in comparison to the supervised approach described above, evaluations were conducted using the same imbalanced test datasets. In addition to image-level labels, ground truth masks were utilized to assess the segmentation performance of each method. Performance metrics of various SOTA unsupervised approaches, applied to modalities: LSM-1, LSM-2 and ASM, are summarized in Tables 5 to 7.

#### 5.3.1 Results

Image-level defect detection performance in LSM-1 across different methods shows substantial variation with MCCs ranging from 0.60 at an FPR of 2.4 % to 0.89 at an FPR of 1.0 %. At the pixel level, minimum PRO-scores ranged from 4.1 to 28.3 %. In general, the low PRO-scores highlight the challenging task of detecting small punctual anomalies such as grid defects in Fig. 2. Common FPs occur at masked border regions or within areas of permitted variations in patterned structures (Fig. 4). The comparison of high pixel-level AUROCs ( $> 99 \%$ ) compared to the measured PRO-scores illustrates their misleading interpretability in imbalanced scenarios.

Efficient-AD demonstrated a 7-fold reduction of FPR, compared to the reconstruction based approach (DDAD) based on denoising diffusion. Thus, Efficient-AD demonstrated an industry-applicable FPR of 0.3 %, with qualitatively precise anomaly segmentations of small pronounced defects. However, despite the patch descriptor's well-defined receptive field ensuring robustness, small defects remain boundary cases and are prone

**Table 5** Defect detection performance of investigated unsupervised approaches (Efficient-AD [Batzner et al. \(2024\)](#), U-Flow [Tialanian et al. \(2024\)](#), GLASS [Chen et al. \(2025\)](#), and DDAD [Mousakhan et al. \(2023\)](#)) on LSM-1. The best-performing method, based on image-level MCC, is highlighted in bold.

Method	AUROC (%)	MCC	Recall (%)	Precision (%)	FPR (%)	AUROC (%)	PRO (%)
image-level						pixel-level	
Efficient-AD	92.6	0.87	82.1	94.0	0.3	80.8	4.1
U-Flow	95.9	0.77	75.8	80.9	1.2	99.1	28.3
GLASS	99.5	<b>0.89</b>	92.6	86.3	1.0	99.2	13.0
DDAD	91.9	0.60	63.2	62.5	2.4	93.7	16.8

**Table 6** Defect detection performance of investigated unsupervised approaches (Efficient-AD [Batzner et al. \(2024\)](#), U-Flow [Tialanian et al. \(2024\)](#), GLASS [Chen et al. \(2025\)](#), and DDAD [Mousakhan et al. \(2023\)](#)) on LSM-2. The best-performing method, based on image-level MCC, is highlighted in bold.

Method	AUROC (%)	MCC	Recall (%)	Precision (%)	FPR (%)	AUROC (%)	PRO (%)
image-level						pixel-level	
Efficient-AD	99.1	<b>0.96</b>	94.8	98.9	0.3	80.9	58.8
U-Flow	99.9	<b>0.96</b>	95.8	97.9	0.5	99.8	95.6
GLASS	99.5	0.94	96.9	93	1.8	99.9	99.2
DDAD	98.2	0.82	84.4	87.1	3.1	99.7	77.9

to misclassification. This is likely due to the bias introduced by ImageNet pretraining and the shallow patch descriptor architecture, which may limit its ability to extract fine-grained, in-domain features for subtle anomalies. In general, small and weakly contrasted point defects remain challenging even in GLASS, resulting in a recall of 92.6 %.

Compared to modality LSM-1, defect classes such as pinholes and pattern misalignments in LSM-2 (Fig. 1 and Fig. 2), which stand out prominently from the background pattern, exhibit more pronounced defect features. Consequently, both image- and pixel-level performance of various unsupervised approaches show improvements, achieving MCCs of up to 0.96 and PRO scores above 99 %.

However, segmentation performance varies significantly across the underlying approaches. Small punctual features are often overestimated or even missed, particularly in embedding-based methods. DDAD demonstrates qualitatively enhanced reconstruction capability, however, it struggles with patches that exhibit large background variations. Although indicating solid segmentation performance, PRO-scores do not consider FP assignments, thus overestimations of defective regions are not directly penalized.

ASM consists of numerous patches containing imperfect masked image borders, due to varying

imaging conditions and the subsequent influence on segmentation performance of the applied deep learning-based model. These artifacts reflect practical deployment conditions and were intentionally retained in the dataset to simulate realistic segmentation imperfections. Additionally, this modality is characterized by large normal feature variations caused by the underlying imaging procedure, which relies on direct reflection.

All approaches exhibited misclassifications in these regions, often leading to TP assignments due to coincidences of real defective areas within the same patch. As a result, despite achieving low performance among all modalities, overestimations of image-level metrics must be considered. In addition to small punctual defects, it was particularly difficult to detect pronounced squeegee strokes among the methods evaluated. However, the anomaly maps (Fig. 5) indicate that the student-teacher based approach Efficient-AD achieved the best qualitative segmentation performance. Again, the localised patch descriptor seems preferable for suppressing false positives.

Above conducted experiments revealed that the defect detection performance of leveraged unsupervised approaches is strongly dependent on dataset properties, determined by its underlying imaging modalities, preprocessing and defect appearance.

**Table 7** Defect detection performance of investigated unsupervised approaches (Efficient-AD [Batzner et al. \(2024\)](#), U-Flow [Tialanian et al. \(2024\)](#), GLASS [Chen et al. \(2025\)](#), and DDAD [Mousakhan et al. \(2023\)](#)) on ASM. The best-performing method, based on image-level MCC, is highlighted in bold.

Method	AUROC (%)	MCC	Recall (%)	Precision (%)	FPR (%)	AUROC (%)	PRO (%)
image-level						pixel-level	
Efficient-AD	85.5	0.31	28.4	38.9	1.7	88.4	4.5
U-Flow	92.4	<b>0.49</b>	52.7	48.8	2.1	89.3	19.9
GLASS	87.4	0.34	48.6	28.6	4.7	82.6	4.0
DDAD	90.9	0.38	55.4	29.7	5.1	96.6	6.5

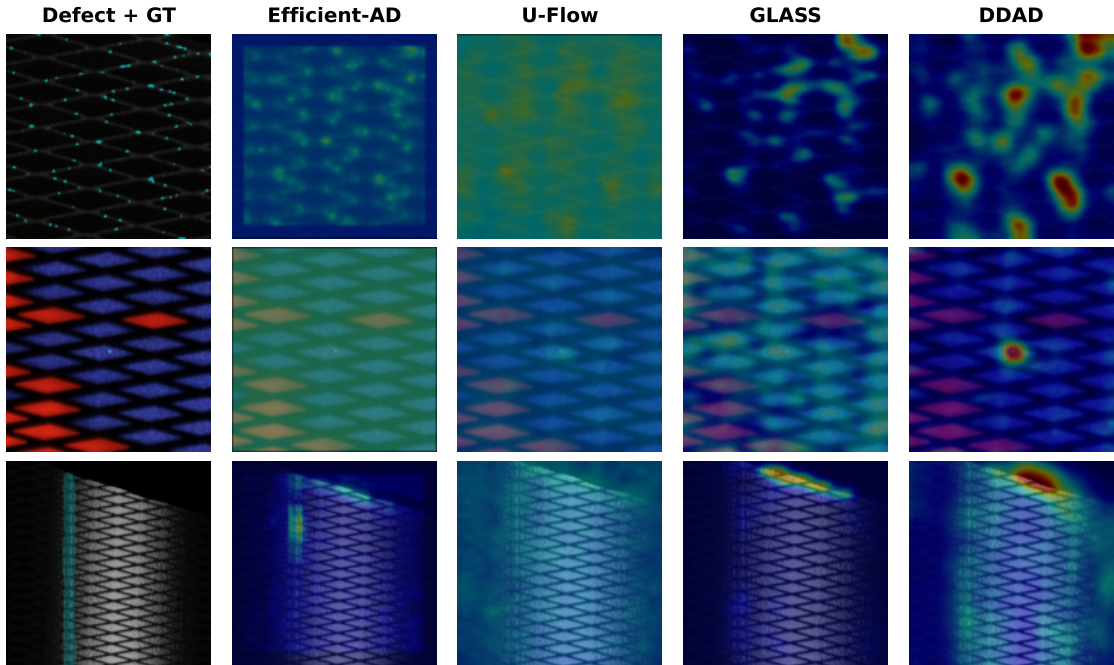


**Fig. 4** Illustration of the pixel-level detection performance (anomaly map overlay) for the evaluated SOTA unsupervised methods (Efficient-AD [Batzner et al. \(2024\)](#), U-Flow [Tialanian et al. \(2024\)](#), GLASS [Chen et al. \(2025\)](#), and DDAD [Mousakhan et al. \(2023\)](#)) on LSM-1, LSM-2, and ASM (top to bottom). The first column displays defects with their ground truth overlays (grid, pinhole, squeegee stroke). Overestimated defect areas (e.g., grid defect) and missed detections of small, low-contrast pinholes demonstrate the challenges of proposed industrial scenario. False positives frequently occur in masked border regions and areas of high contrast variations, as observed in ASM (bottom row).

Showing distinct defective feature characteristics, LSM-2 achieved best overall performance, resulting in industrial applicable FPR of Efficient-AD and U-Flow, although struggling with weakly contrasted pinholes. Compared to the supervised approach in section 4.1, FPRs are mostly significantly higher (up to factor 10 in ASM), limiting industrial applicability, particularly in the case of ASM.

Despite DDAD’s qualitatively good reconstruction capability, modelling permitted pattern variations and patterns in border regions was often

not feasible (Fig. 6). In addition, DDAD exhibited reconstruction instabilities resulting in noise that increased with higher domain adaptation weightings.

### 5.3.2 Limitations

The evaluations of these approaches should be considered as estimations based on the chosen methods parameters, preprocessing techniques, and training settings, including random seeds. Extensive hyperparameter tuning and

advanced preprocessing strategies are left for future research.

## 6 Conclusions and Outlook

This publication introduces a novel surface defect detection dataset that exhibits a “real-world” industrial use case. The investigated screen-printed samples were captured using three different optical modalities. Typical for industrial inspection, the dataset reflects imperfect imaging conditions caused by imaging modalities, data preprocessing, and permitted sample variations, thereby presenting challenges for defect detection algorithms. In addition to extending common unsupervised settings, the dataset includes large-scale supervised training data, comprising tens of thousands of fault-free patches. Based on a review of recent literature, the proposed dataset can be assumed to be the largest publicly available, enabling research on both unsupervised and supervised approaches by using both synthetic and real defects.

It was observed that SOTA unsupervised methods, which achieve remarkable performance on established benchmark datasets such as MVTec [Bergmann et al. \(2021\)](#), struggled in these specific industrial scenarios. The occurrence of small and weakly contrasted defects, combined with high permitted design variability, significantly limited defect detection performance, especially at the pixel level. Among the evaluated methods, the most promising approaches are based on defect synthetization at both the feature and image-levels and knowledge distillation using patch descriptor networks, achieving image-level MCCs of up to 0.89 in LSM-1 and 0.96 in LSM-2. However, despite robust performance of Efficient-AD [Batzner et al. \(2024\)](#) with industry-applicable low FPRs in LSM-1 and LSM-2, weakly contrasted defects remained challenging. While certain unsupervised approaches have shown promising advances in image-level detection performance for specific imaging modalities (e.g., LSM-2), future research should focus enhancing segmentation performance under industrial imaging conditions.

Incorporating available weakly labeled defective samples within a mixed supervised training strategy is able to improve image-level defect detection performance by large margins. The

experiments described in Section 5.2 indicate that the initial comprehensive feature distribution, by means of several tens of thousands of synthesized punctual defects, is complemented and made more diverse, even with small amounts of available real defects. The injection of small fractions (9 samples in ASM) of previously unseen defect classes (area defects) substantially improved model generalization. These results indicate that previously unseen defects, such as those that could not be synthesized, can provide strong learning signals, helping to refine the decision boundary.

The defect detection performance of small and weakly contrasted point defects was substantially improved with mixed training ( $MCC = 0.96$  in LSM-1), compared to training solely on real defects ( $MCC = 0.91$ ) using a standard ResNet-18 backbone. Notably, in the few-shot regime, the mixed supervised strategy showed substantial performance gains compared to pure oversampling across various backbones (ResNet-18, ResNet-50, EfficientNet-B0, EfficientNet-B4, and ConvNeXt-Tiny). More recent backbones, such as ConvNeXt-Tiny, achieved a high MCC of up to 0.96 with only 10 real injected defects.

These findings suggest a valuable capability for industrial applications, as emerging defects, both seen and previously unseen, can be efficiently integrated into subsequent scalable training, enhancing overall feature diversity. Thus, initial training on synthetic defects can be incrementally improved, meeting process requirements such as a low FPR and high recall.

Furthermore, purely synthetic training achieved near-optimal ( $MCCs$  up to 0.99) defect detection performance in modalities that exhibit distinct feature characteristics, such as pinholes in LSM-2. Purely synthetic training outperformed SOTA unsupervised approaches in two out of three modalities (LSM-2 and ASM; ResNet-18).

Despite promising investigations of generalization capabilities with a limited number of available defective samples, further experiments are necessary for deeper insights. These should involve more diverse defect classes and varying hyperparameters, such as the injection probability  $p_{inj}$  of real defects. The selected injection probability of 1/32 was intended to avoid overfitting to injected real defect characteristics. However, in some cases—depending on defect availability and diversity, the defect synthesis approach, or

the imaging modality (e.g., ASM)—higher injection probabilities may be preferable to align the decision boundary more closely with the incorporated defect features. Furthermore, in future work, defect selection strategies inspired by active learning frameworks [Gao et al. \(2025\)](#) could be considered, as higher fractions of real defects appear to saturate performance in certain cases. Therefore, injected diversity seems to be more important than the absolute quantity of defective data.

Additionally, permitted normal data variations are learned through large amounts (50 000 – 100 000 of augmented fault-free patches, even with noisy labels. Noisy labels, due to e.g. process contamination during the image acquisition, were estimated to account for 2 – 5 % in LSM-1. These corrupted labels did not show a significant impact during training. This observation is consistent with unsupervised and supervised learning paradigms: unsupervised methods rely on clean normal data to enable the modeling of compact representations, whereas supervised methods are able to learn a robust decision boundary even in the presence of noisy labels [Bar, Drory, and Giryes \(2022\)](#). Regarding our approach, this can be explained by the large-scale balanced data streams, including a diverse set of permitted fault-free data variations, helping the model to learn what patterns are considered normal.

Thus, the screening effort of fault-free data in the proposed unsupervised training datasets could be considered more elaborate than the presented supervised data preprocessing workflow in [Krassnig et al. \(2024\)](#), minimizing manual labeling effort to known defective sample regions. Thus, further research should focus on efficient and industrial applicable data preparation and preprocessing workflows within unsupervised and supervised approaches and the influence of different proportions of noisy labels. As a direct implication of above findings, research in self-supervised approaches that utilize these large-scale normal data distributions should be emphasized to enhance industry-applicable model robustness at low labeling costs.

In summary, the mixed supervised training strategy [Haselmann M. , Krassnig, P. J., and Gruber D. P. \(2022\)](#), based on the efficient preprocessing workflow proposed in [Krassnig et al. \(2024\)](#), is capable of fulfilling industrial inspection requirements with minimized labeling effort.

Labeling is restricted to known defective samples and regions, as the extraction of fault-free patches is integrated into an automated procedure. The model-free synthetization algorithm enables defect generation without requiring elaborate learning of defect distributions. Complementary defect features are learned through the injection of a small set of weakly labeled real defects, enabling model generalization. However, recent zero-shot and few-shot anomaly synthesis approaches [Lai et al. \(2025\)](#); [Shin, Jeong, and Heo \(2025\)](#); [Sun, Cao, Dong, and Fink \(2025\)](#) may be preferable in future adaptations, further enhancing defect realism and diversity within the synthetic baseline.

Based on our findings, we raise the question of whether defining industrial anomaly detection as a fully open-set problem is appropriate in common real-world manufacturing processes. Since defect causes are often known in advance, a reformulated paradigm such as the proposed restricted open-set problem may offer a more practically applicable definition for industrial scenarios. Future work may explore this direction in more detail, particularly in terms of formalizing such paradigms and resulting learning strategies, and evaluating them under realistic industrial constraints.

## 6.1 Future Applications

The proposed dataset is designed to advance future research on both unsupervised and supervised approaches suitable for challenging industrial anomaly detection use cases. Leveraging the proposed dataset enables further exploration in the following directions:

- Investigation of the impact of increased normal feature variations on the robustness of unsupervised approaches by utilizing larger sets of fault-free training samples than those used in the proposed experiments. Additionally, an examination of the effect of real noisy labels by applying the “unscreened” automatically extracted fault-free training data.
- Conduction of research on self-supervised learning approaches [Hojjati, Ho, and Armanfard \(2024\)](#) utilizing the synthetic or fault-free large-scale training sets. Therefore, feature extractors of unsupervised approaches, such as described in [Koshil, Wegener, Mentrup, Frintrop, and](#)

Wilms (2024); Liang et al. (2024), could be pre-trained to learn more discriminative features of the target domain.

- Foster research on zero-shot or few-shot defect synthesis approaches like recent works Lai et al. (2025); Shin et al. (2025); Sun et al. (2025); X. Zhang, Xu, and Zhou (2024) that may enable rapid initial deployment in industrial scenarios. Therefore, the additional fault-free data in ISP-AD can serve as a research basis.
- Encouraging research on methods that integrate both synthetic and real defects during training, as demonstrated by the proposed mixed supervised training and recent supervised anomaly detection methods.

**Acknowledgements.** The research work was performed within the COMET-project: Deep online learning for highly adaptable polymer surface inspection systems (project-no.: 879785) at the Polymer Competence Center Leoben GmbH (PCCL, Austria) within the framework of the COMET-program of the Federal Ministry for Climate Action, Environment, Energy, Mobility, Innovation and Technology and the Federal Ministry for Digital and Economic Affairs and with contributions by Burg Design GmbH. The PCCL is funded by the Austrian Government and the State Governments of Styria, Lower Austria and Upper Austria.

**Funding.** Open access publishing enabled by Montanuniversität Leoben agreement with Springer Nature (Austria KEMÖ: Springer Transformative Agreement). This work was supported within the COMET-project (project-no.: 879785).

**Data availability.** The dataset supporting this research is publicly available on Zenodo at <https://doi.org/10.5281/zenodo.14911042>, and is licensed under the Creative Commons Attribution-NonCommercial-ShareAlike 4.0 International (CC BY-NC-SA 4.0).

**Author contribution.** Conceptualization: PJK and DPG; Methodology: PJK; Formal analysis and investigation: PJK; Writing - original draft preparation: PJK; Writing - review and editing: PJK and DPG; Funding acquisition: DPG; Supervision: DPG.

## Declarations

**Competing interests.** The authors have no competing interests to declare that are relevant to the content of this article.

## Appendix A

Table 7 illustrates the training and test data splits of the proposed ISP-AD dataset. The augmentation settings applied to the supervised training data are shown in Table 8. In addition to the presented data splits, large-scale fault-free training data (10 000 - 20 000 patches) without augmentation is made available for all three modalities: LSM-1, LSM-2, and ASM. As outlined in Section 3.2, the extracted patches can be considered noisy. The naming convention of image-level labels within the .hdf5 files follows:

- Stream including both fault-free and synthetic defects: **syn\_stream**
- Ground truth masks: **ground\_truth**

To reproduce the experiments presented in Section 5.2, randomly sampled fractions of the mixed, area, and points defect groups will be made available separately.

**Table 7** Overview of the available data splits in the proposed ISP-AD dataset. The dataset is divided into unsupervised training data, containing screened fault-free patches, and supervised training data, which includes "noisy" fault-free patches along with additional synthetic and real defective data. Test splits remain the same for both settings, mimicking the imbalanced data distributions typical of industrial inspection. Additional unaugmented fault-free data available is not included in this listing.

Modality	Train					Test		
	Unsupervised		Supervised			Super- / Unsupervised		
	#Good	#Good	#Synthetic	#Area	#Points	#Good	#Area	#Points
LSM-1	3678	100 669	99 331	120	52	1470	49	46
LSM-2	401	50 036	49 964	62	66	382	63	33
ASM	500	103 622	96 369	37	109	1916	33	41

**Table 8** Augmentation settings of generated supervised training set including random affine and illumination transformations.

Modality	Affine Transformations					Illumination Transformations	
	Rotation	Scale	Shear	Vertical Flip	Horizontal Flip	Brightness	Contrast
LSM-1	45.0	(0.90,1.10)	10.0	yes	yes	(0.75,1.25)	(0.75,1.25)
LSM-2	45.0	(0.90,1.10)	20.0	yes	yes	(0.75,1.25)	(0.75,1.25)
ASM	10.0	(1.0,1.2)	10.0	yes	yes	no	no

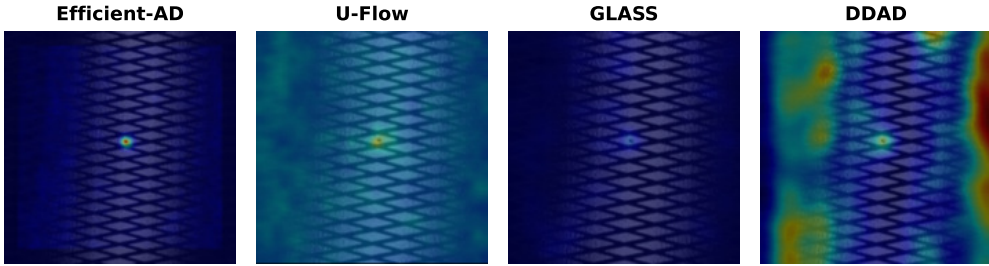


**Fig. 5** Visualization of the pixel-level detection performance (anomaly map overlay) for the investigated unsupervised methods (Efficient-AD [Batzner et al. \(2024\)](#), U-Flow [Talianian et al. \(2024\)](#), GLASS [Chen et al. \(2025\)](#), and DDAD [Mousakhan et al. \(2023\)](#)) on ASM. Efficient-AD demonstrated the most accurate detection of the depicted punctual defect. The reconstruction-based approach DDAD produced a high number of false positive detections in transmission areas of direct reflection and masked border regions.

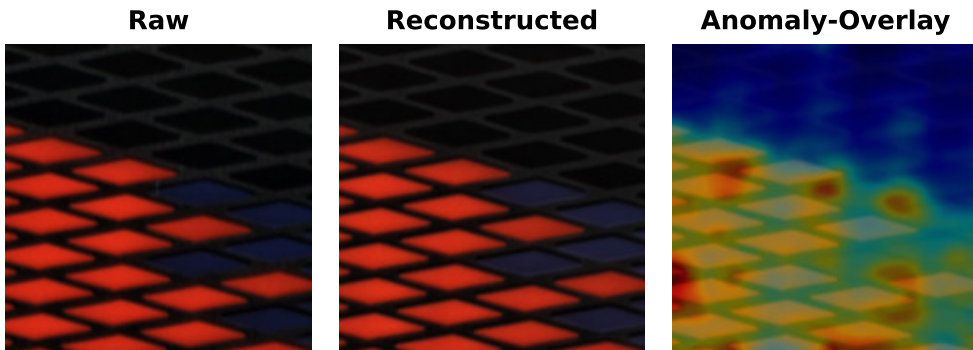


**Fig. 6** Illustration of the reconstruction capabilities of DDAD [Mousakhan et al. \(2023\)](#) on a patterned surface of LSM-1. The denoising diffusion process enabled a qualitatively good reconstruction, effectively omitting the small fiber in the raw image. However, fine-grained details, such as contrast variations in the grid regions, remained challenging, resulting in high anomaly scores across broad areas.

## References

Akcay, S., Ameln, D., Vaidya, A., Lakshmanan, B., Ahuja, N., Genc, U. (2022). Anomalib: A deep learning library for anomaly detection. *2022 ieee international conference on image processing (icip)* (p. 1706-1710).

Alzarooni, A., Iqbal, E., Khan, S.U., Javed, S., Moyo, B., Abdulrahman, Y. (2025). Anomaly detection for industrial applications, its challenges, solutions, and future directions: A review. *arXiv preprint arXiv:2501.11310*, , <https://doi.org/10.48550/arXiv.2501.11310>

Bai, D., Li, G., Du Jiang, Yun, J., Tao, B., Jiang, G., ... Ju, Z. (2024). Surface defect detection methods for industrial products with imbalanced samples: A review of progress in the 2020s. *Engineering Applications of Artificial Intelligence*, 130, 107697, <https://doi.org/10.1016/j.engappai.2023.107697>

Baitieva, A., Hurych, D., Besnier, V., Bernard, O. (2024). Supervised anomaly detection for complex industrial images. *2024 ieee/cvf conference on computer vision and pattern recognition (cvpr)* (pp. 17754-17762).

Bao, T., Chen, J., Li, W., Wang, X., Fei, J., Wu, L., ... Zheng, Y. (2023). Miad: A maintenance inspection dataset for unsupervised anomaly detection. *2023 ieee/cvf international conference on computer vision workshops (iccvw)* (pp. 993-1002). IEEE.

Bar, O., Drory, A., Giryes, R. (2022). A spectral perspective of dnn robustness to label noise. *International conference on artificial intelligence and statistics* (pp. 3732-3752).

Batzner, K., Heckler, L., König, R. (2024). Efficientad: Accurate visual anomaly detection at millisecond-level latencies. *2024 ieee/cvf winter conference on applications of computer vision (wacv)*. IEEE.

Berg, S., Kutra, D., Kroeger, T., Straehle, C.N., Kausler, B.X., Haubold, C., ... Kreshuk, A. (2019). ilastik: interactive machine learning for (bio)image analysis. *Nature Methods*, 16(12), 1226-1232, <https://doi.org/10.1038/s41592-019-0582-9>

Bergmann, P., Batzner, K., Fauser, M., Sattlegger, D., Steger, C. (2021). The mvtec anomaly detection dataset: a comprehensive real-world dataset for unsupervised anomaly detection. *International Journal of Computer Vision*, 129(4), 1038-1059, <https://doi.org/10.1007/s11263-020-01400-4>

Bergmann, P., Fauser, M., Sattlegger, D., Steger, C. (2020). Uninformed students: Student-teacher anomaly detection with discriminative latent embeddings. *2020 ieee/cvf conference on computer vision and pattern recognition (cvpr)* (p. 4182-4191).

Bergmann, P., Löwe, S., Fauser, M., Sattlegger, D., Steger, C. (2019). Improving unsupervised defect segmentation by applying structural similarity to autoencoders. *Proceedings of the 14th international joint conference on computer vision, imaging and computer graphics theory and applications (visigraapp 2019) - volume 5: Visapp* (p. 372-380).

Biegeleisen, J.I. (2012). *Complete book of silk screen printing production*. Dover Publications. Retrieved from <https://books.google.at/books?id=o8sKJSHeUMC>

Božič, J., Tabernik, D., Skočaj, D. (2021). Mixed supervision for surface-defect detection: From weakly to fully supervised learning. *Computers in Industry*, 129, 103459, <https://doi.org/https://doi.org/10.1016/j.compind.2021.103459>

Cao, Y., Xu, X., Liu, Z., Shen, W. (2023). Collaborative discrepancy optimization for reliable image anomaly localization. *IEEE Transactions on Industrial Informatics*, 19(11), 10674-10683, <https://doi.org/10.1109/TII.2023.3241579>

Chen, Q., Luo, H., Lv, C., Zhang, Z. (2025). A unified anomaly synthesis strategy with gradient ascent for industrial anomaly detection and localization. *Computer vision – eccv 2024* (pp. 37–54). Springer Nature Switzerland.

Cheng, Y., Cao, Y., Chen, R., Shen, W. (2024). Rad: A comprehensive dataset for benchmarking the robustness of image anomaly detection. *arXiv preprint arXiv:2406.07176*, , <https://doi.org/10.48550/arXiv.2406.07176>

Chin, R.T., & Harlow, C.A. (1982). Automated visual inspection: A survey. *IEEE Transactions on Pattern Analysis and Machine Intelligence, PAMI-4*(6), 557-573, <https://doi.org/10.1109/TPAMI.1982.4767309>

Cimpoi, M., Maji, S., Kokkinos, I., Mohamed, S., Vedaldi, A. (2014). Describing textures in the wild. *2014 ieee conference on computer vision and pattern recognition* (pp. 3606–3613). IEEE.

Cui, Y., Liu, Z., Lian, S. (2023). A survey on unsupervised anomaly detection algorithms for industrial images. *IEEE Access*, 11, 55297-55315, <https://doi.org/10.1109/ACCESS.2023.3282993>

Denninger, M., Sundermeyer, M., Winkelbauer, D., Zidan, Y., Olefir, D., Elbadrawy, M., ... Katam, H. (2019). Blenderproc. *arXiv preprint arXiv:1911.01911*, , <https://doi.org/10.48550/arXiv.1911.01911>

Dey, B., De Ridder, V., Blanco, V., Halder, S., Van Waeyenberge, B. (2024). Addressing class imbalance and data limitations in advanced node semiconductor defect inspection: A generative approach for sem images. *2024 international symposium elmar* (p. 141-148).

Ding, C., Pang, G., Shen, C. (2022). Catching both gray and black swans: Open-set supervised anomaly detection. *Proceedings of the ieee/cvf conference on computer vision and pattern recognition (cvpr)* (p. 7388-7398).

Dosovitskiy, A. (2020). An image is worth 16x16 words: Transformers for image recognition at scale. *arXiv preprint arXiv:2010.11929*, , <https://doi.org/10.48550/arXiv.2010.11929>

Duan, Y., Hong, Y., Niu, L., Zhang, L. (2023). Few-shot defect image generation via defect-aware feature manipulation. *Proceedings of the AAAI Conference on Artificial Intelligence*, 37(1), 571–578, <https://doi.org/10.1609/aaai.v37i1.25132>

Gao, S., Jiang, Y., Xia, T., Li, Y., Zhu, Y., Xi, L. (2025). A multi-stage active learning framework with an instance-based sample selection algorithm for steel surface defect. *Advanced Engineering Informatics*, 64, 103080, <https://doi.org/https://doi.org/10.1016/j.aei.2024.103080> Retrieved from <https://www.sciencedirect.com/science/article/pii/S14740340>

Gui, G., Gao, B.-B., Liu, J., Wang, C., Wu, Y. (2025). Few-shot anomaly-driven generation for anomaly classification and segmentation. A. Leonardis, E. Ricci, S. Roth, O. Russakovsky, T. Sattler, & G. Varol (Eds.), *Computer vision – eccv 2024* (pp. 210–226). Springer Nature Switzerland.

Haselmann, M., & Gruber, D. (2017). Supervised machine learning based surface inspection by synthetizing artificial defects. *2017 16th ieee international conference on machine learning and applications (icmla)* (pp. 390–395). IEEE.

Haselmann M. , Krassnig, P. J., and Gruber D. P. (2022). Visual inspection of patterned surfaces with supervised deep learning using both real and synthetic defects. *Advances in Signal Processing and Artificial Intelligence: Proceedings of the 4th International Conference on Advances in Signal Processing and Artificial Intelligence 19-21 October 2022 Corfu, Greece, ,* <https://doi.org/10.13140/RG.2.2.10749.13281>

He, K., Zhang, X., Ren, S., Sun, J. (2016). Deep residual learning for image recognition. *2016 ieee conference on computer vision and pattern recognition (cvpr)*. IEEE.

He, X., Luo, Z., Li, Q., Chen, H., Li, F. (2023). Dg-gan: A high quality defect image generation method for defect detection. *Sensors*, 23(13), , <https://doi.org/10.3390/s23135922>

Hojjati, H., Ho, T.K.K., Armanfard, N. (2024). Self-supervised anomaly detection in computer vision and beyond: A survey and outlook. *Neural Networks*, 172, 106106, <https://doi.org/10.1016/j.neunet.2024.106106>

Hu, T., Zhang, J., Yi, R., Du, Y., Chen, X., Liu, L., ... Wang, C. (2024, Mar.). Anomalydiffusion: Few-shot anomaly image generation with diffusion model. *Proceedings of the AAAI Conference on Artificial Intelligence*, 38(8), 8526-8534, <https://doi.org/10.1609/aaai.v38i8.28696>

Huang, K., Zeng, Y., Zhao, J., Chai, S., Yang, F. (2025). Weakly supervised complex texture defect detection based on nested u-net architecture. *Journal of Nondestructive Evaluation*, 44(1), 24, <https://doi.org/https://doi.org/10.1007/s10921-025-01161-5>

Jha, S.B., & Babiceanu, R.F. (2023). Deep cnn-based visual defect detection: Survey of current literature. *Computers in Industry*, 148, 103911, <https://doi.org/10.1016/j.compind.2023.103911>

Jia Deng, Wei Dong, Socher, R., Li-Jia Li, Kai Li, Li Fei-Fei. (2009). Imagenet: A large-scale hierarchical image database. *2009 ieee conference on computer vision and pattern recognition*. IEEE.

Koshil, M., Wegener, T., Mentrup, D., Frintrop, S., Wilms, C. (2024). Anomalouspatchcore: Exploring the use of anomalous samples in industrial anomaly detection. *arXiv preprint arXiv:2408.15113*, , <https://doi.org/10.48550/arXiv.2408.15113>

Kozamernik, N., & Bračun, D. (2025). A novel fuseddecode autoencoder for industrial visual inspection: Incremental anomaly detection improvement with gradual transition from unsupervised to mixed-supervision learning with reduced human effort. *Computers in Industry*, 164, 104198, <https://doi.org/10.1016/j.compind.2024.104198>

Krassnig, P.J., Haselmann, M., Kremnitzer, M., Gruber, D.P. (2024). Efficient surface defect detection in industrial screen printing with minimized labeling effort. *Integrated Computer-Aided Engineering*, 32(1), 1–21, <https://doi.org/10.3233/ICA-240742>

Krassnig, P. J., Haselmann M., and Gruber D. P. (2022). Inspection approach for automated in-line defect detection on decorated foil plates. *Advances in Signal Processing and Artificial Intelligence: Proceedings of the 4th International Conference on Advances in Signal Processing and Artificial Intelligence 19-21 October 2022 Corfu, Greece*, , <https://doi.org/10.13140/RG.2.2.10749.13281>

Kujawińska, A., & Vogt, K. (2015). Human factors in visual quality control. *Management and Production Engineering Review*, 6(2), 25–31, <https://doi.org/10.1515/mper-2015-0013>

Lai, Z., Lu, Y., Li, X., Lin, J., Qu, Y., Cao, L., ... Ji, R. (2025). Anomalypainter: Vision-language-diffusion synergy for zero-shot realistic and diverse industrial anomaly synthesis. *arXiv preprint arXiv:2503.07253*, , <https://doi.org/https://doi.org/10.48550/arXiv.2503.07253>

LeCun, Y., Bengio, Y., Hinton, G. (2015). Deep learning. *Nature*, 521(7553), 436–444, <https://doi.org/10.1038/nature14539>

Lee, S., Lee, S., Song, B.C. (2022). CfA: Coupled-hypersphere-based feature adaptation for target-oriented anomaly localization. *IEEE Access*, 10, 78446–78454, <https://doi.org/10.1109/access.2022.3193699>

Li, C.-L., Sohn, K., Yoon, J., Pfister, T. (2021, June). Cutpaste: Self-supervised learning for anomaly detection and localization. *Proceedings of the ieee/cvpr conference on computer vision and pattern recognition (cvpr)* (p. 9664-9674).

Liang, Y., Hu, Z., Huang, J., Di, D., Su, A., Fan, L. (2024). Tocoad: Two-stage contrastive learning for industrial anomaly detection. *arXiv preprint arXiv:2407.01312*, , <https://doi.org/10.48550/arXiv.2407.01312>

Liu, J., Xie, G., Wang, J., Li, S., Wang, C., Zheng, F., Jin, Y. (2024). Deep industrial image anomaly detection: A survey. *Machine Intelligence Research*, 21(1), 104–135, <https://doi.org/10.1007/s11633-023-1459-z>

Liu, Z., Mao, H., Wu, C.-Y., Feichtenhofer, C., Darrell, T., Xie, S. (2022, June). A convnet for the 2020s. *Proceedings of the ieee/cvpr conference on computer vision and pattern recognition (cvpr)* (p. 11976-11986).

Liu, Z., Zhou, Y., Xu, Y., Wang, Z. (2023). Simplanet: A simple network for image anomaly detection and localization. *2023 ieee/cvpr conference on computer vision and pattern recognition (cvpr)* (pp. 20402–20411). IEEE.

Lohweg, V. (2023). *Bildverarbeitung in der automation* (Vol. 17). Berlin, Heidelberg: Springer Berlin Heidelberg.

Loshchilov, I., & Hutter, F. (2016). Sgdr: Stochastic gradient descent with warm restarts. *arXiv e-prints*, , <https://doi.org/10.48550/arXiv.1608.03983>

Matthias Wieler, F.A.H., Tobias Hahn (2007). *Weakly supervised learning for industrial optical inspection*. Retrieved 13.02.2025, from <https://hci.iwr.uni-heidelberg.de/content/weakly-supervised-learning-industrial-optical-inspection>

Mishra, P., Verk, R., Fornasier, D., Piciarelli, C., Foresti, G.L. (2021). Vt-adl: A vision transformer network for image anomaly detection and localization. *2021 ieee 30th international symposium on industrial electronics (isie)*. IEEE.

Mousakhan, A., Brox, T., Tayyub, J. (2023). Anomaly detection with conditioned denoising diffusion models. *arXiv preprint arXiv:2305.15956*, , <https://doi.org/10.48550/arXiv.2305.15956>

Pérez, P., Gangnet, M., Blake, A. (2023). Poisson image editing. , 577–582, <https://doi.org/10.1145/3596711.3596772>

Perlin, K. (1985). An image synthesizer. *ACM SIGGRAPH Computer Graphics*, 19(3), 287–296, <https://doi.org/10.1145/325165.325247>

Perlin, K. (2002). Improving noise. *ACM Transactions on Graphics*, 21(3), 681–682, <https://doi.org/10.1145/566654.566636>

Pierre Gutierrez, Maria Luschkova, Antoine Cordier, Mustafa Shukor, Mona Schappert, Tim Dahmen. (2021). Synthetic training data generation for deep learning based quality inspection. (pp. 9–16). SPIE.

Posilović, L., Medak, D., Subasic, M., Budimir, M., Loncaric, S. (2021). Generative adversarial network with object detector discriminator for enhanced defect detection on ultrasonic b-scans. *Neurocomputing*, 459(11), 361–369, <https://doi.org/10.1016/j.neucom.2021.06.094>

Prunella, M., Scardigno, R.M., Buongiorno, D., Brunetti, A., Longo, N., Carli, R., ... Bevilacqua, V. (2023). Deep learning for automatic vision-based recognition of industrial surface defects: A survey. *IEEE Access*, 11, 43370–43423, <https://doi.org/10.1109/ACCESS.2023.3271748>

Raisul Islam, M., Zakir Hossain Zamil, M., Eshammam Rayed, M., Mohsin Kabir, M., Mridha, M.F., Nishimura, S., Shin, J. (2024). Deep learning and computer vision techniques for enhanced quality control in manufacturing processes. *IEEE Access*, 12, 121449–121479, <https://doi.org/10.1109/ACCESS.2024.3453664>

Ren, Z., Fang, F., Yan, N., Wu, Y. (2022). State of the art in defect detection based on machine vision. *International Journal of Precision Engineering and Manufacturing-Green Technology*, 9(2), 661–691, <https://doi.org/10.1007/s40684-021-00343-6>

Rolih, B., Fučka, M., Skočaj, D. (2025). Super-simplenet: Unifying unsupervised and supervised learning for fast and reliable surface defect detection. *Pattern recognition* (pp. 47–65). Springer Nature Switzerland.

Ronneberger, O., Fischer, P., Brox, T. (2015). U-net: Convolutional networks for biomedical image segmentation. (pp. 234–241). Springer, Cham.

Roth, K., Pemula, L., Zepeda, J., Scholkopf, B., Brox, T., Gehler, P. (2022). Towards total recall in industrial anomaly detection. *2022 ieee/cvf conference on computer vision and pattern recognition (cvpr)* (pp. 14298–14308). IEEE.

Rudolph, M., Wehrbein, T., Rosenhahn, B., Wandt, B. (2023). Asymmetric student-teacher networks for industrial anomaly detection. *2023 ieee/cvf winter conference on applications of computer vision (wacv)* (pp. 2591–2601). IEEE.

Saberironaghi, A., Ren, J., El-Gindy, M. (2023). Defect detection methods for industrial products using deep learning techniques: A review. *Algorithms*, 16(2), 95, <https://doi.org/10.3390/a16020095>

Sauer, M., Meilchen, S., Kalleder, A., Mennig, M., Schmidt, H. (2011). Screen printing. M.A. Aegerter (Ed.), *Sol gel technologies for glass producers and users* (pp. 117–122). New York, NY: Springer Science + Business Media. Retrieved from [https://link.springer.com/chapter/10.1007/978-0-387-88953-5\\_14](https://link.springer.com/chapter/10.1007/978-0-387-88953-5_14)

Schlüter, H.M., Tan, J., Hou, B., Kainz, B. (2022). Natural synthetic anomalies for self-supervised anomaly detection and localization. *Computer vision – eccv 2022* (pp. 474–489). Springer Nature Switzerland.

Shin, M., Jeong, S., Heo, Y.S. (2025). Anodapter: A unified framework for generating aligned anomaly images and masks using diffusion models. *IEEE Access*, 13, 83483-83504, <https://doi.org/10.1109/ACCESS.2025.3568866>

Sun, H., Cao, Y., Dong, H., Fink, O. (2025, June). Unseen visual anomaly generation. *Proceedings of the ieee/cvf conference on computer vision and pattern recognition (cvpr)* (p. 25508-25517).

Tailanian, M., Pardo, Á., Musé, P. (2024). U-flow: A u-shaped normalizing flow for anomaly detection with unsupervised threshold. *Journal of Mathematical Imaging and Vision*, 66(4), 678–696, <https://doi.org/10.1007/s10851-024-01193-y>

Tan, M., & Le, Q. (2019, 09–15 Jun). EfficientNet: Rethinking model scaling for convolutional neural networks. K. Chaudhuri & R. Salakhutdinov (Eds.), *Proceedings of the 36th international conference on machine learning* (Vol. 97, pp. 6105–6114). PMLR. Retrieved from <https://proceedings.mlr.press/v97/tan19a.html>

Tebbe, J., & Tayyub, J. (2024, June). Dynamic addition of noise in a diffusion model for anomaly detection. *Proceedings of the ieee/cvf conference on computer vision and pattern recognition (cvpr) workshops* (p. 3940-3949).

Thomine, S., & Snoussi, H. (2024). Distillation-based fabric anomaly detection. *Textile Research Journal*, 94(5-6), 552–565, <https://doi.org/10.1177/00405175231206820>

Tien, T.D., Nguyen, A.T., Tran, N.H., Huy, T.D., Duong, S.T., Nguyen, C.D.T., Truong, S.Q.H. (2023, June). Revisiting reverse distillation for anomaly detection. *Proceedings of the ieee/cvf conference on computer vision and pattern recognition (cvpr)* (p. 24511-24520).

Wang, C., Zhu, W., Gao, B.-B., Gan, Z., Zhang, J., Gu, Z., ... Ma, L. (2024). Real-iad: A real-world multi-view dataset for benchmarking versatile industrial anomaly detection. *2024 ieee/cvf conference on computer vision and pattern recognition (cvpr)* (pp. 22883–22892). IEEE.

Wang, S., Hu, Y., Liu, X., Wang, S., Wang, G., Xu, C., ... Chen, P. (2025). “stones from other hills can polish jade”: Zero-shot anomaly image synthesis via cross-domain anomaly injection. *arXiv preprint arXiv:2501.15211*, , <https://doi.org/https://doi.org/10.48550/arXiv.2501.15211>

Wen, L., Zhang, Y., Hu, W., Li, X. (2024). The survey of industrial anomaly detection for industry 5.0. *International Journal of Computer Integrated Manufacturing*, 1–22, <https://doi.org/10.1080/0951192X.2024.2397821>

Xie, G., Wang, J., Liu, J., Zheng, F., Jin, Y. (2023). Pushing the limits of fewshot anomaly detection in industry vision: Graphcore. *arXiv preprint arXiv:2301.12082*, , <https://doi.org/10.48550/arXiv.2301.12082>

Xu, X., Wang, Y., Huang, Y., Liu, J., Lei, X., Xie, G., ... Lu, Z. (2025). A survey on industrial anomalies synthesis. *arXiv preprint arXiv:2502.16412*, , <https://doi.org/https://doi.org/10.48550/arXiv.2502.16412>

Yao, X., Li, R., Zhang, J., Sun, J., Zhang, C. (2023, June). Explicit boundary guided semi-push-pull contrastive learning for supervised anomaly detection. *Proceedings of the ieee/cvf conference on computer vision and pattern recognition (cvpr)* (p. 24490-24499).

Yu, J., Zheng, Y., Wang, X., Li, W., Wu, Y., Zhao, R., Wu, L. (2021). Fastflow: Unsupervised anomaly detection and localization via 2d normalizing flows. *arXiv preprint arXiv:2111.07677*, , <https://doi.org/10.48550/arXiv.2111.07677>

Zavrtanik, V., Kristan, M., Skočaj, D. (2022). Dsr – a dual subspace re-projection network for surface anomaly detection. S. Avidan, G. Brostow, M. Cissé, G.M. Farinella, & T. Hassner (Eds.), *Computer vision – eccv 2022* (pp. 539–554). Springer Nature Switzerland.

Zavrtanik, V., Kristan, M., Skočaj, D. (2021, October). Draem - a discriminatively trained reconstruction embedding for surface anomaly detection. *Proceedings of the ieee/cvf international conference on computer vision (iccv)* (p. 8330-8339).

Zhang, H., Wang, Z., Wu, Z., Jiang, Y.-G. (2023). Diffusionad: Norm-guided one-step denoising diffusion for anomaly detection. *arXiv preprint arXiv:2303.08730*, , <https://doi.org/10.48550/arXiv.2303.08730>

Zhang, H., Wu, Z., Wang, Z., Chen, Z., Jiang, Y.-G. (2023). Prototypical residual networks for anomaly detection and localization. *2023 ieee/cvf conference on computer vision and pattern recognition (cvpr)* (p. 16281-16291).

Zhang, L., Dai, Y., Fan, F., He, C. (2022). Anomaly detection of gan industrial image based on attention feature fusion. *Sensors*, 23(1), 355, <https://doi.org/10.3390/s23010355>

Zhang, X., Xu, M., Zhou, X. (2024). Realnet: A feature selection network with realistic synthetic anomaly for anomaly detection. *Proceedings of the ieee/cvf conference on computer vision and pattern recognition* (pp. 16699–16708).

Zheng, X., Zheng, S., Kong, Y., Chen, J. (2021). Recent advances in surface defect inspection of industrial products using deep learning techniques. *The International Journal of Advanced Manufacturing Technology*, 113(1-2), 35–58, <https://doi.org/10.1007/s00170-021-06592-8>

Zhong, X., Zhu, J., Liu, W., Hu, C., Deng, Y., Wu, Z. (2023). An overview of image generation of industrial surface defects. *Sensors*, 23(19), , <https://doi.org/10.3390/s23198160>

Zhou, Y., Xu, X., Song, J., Shen, F., Shen, H.T. (2024). Msflow: Multiscale flow-based framework for unsupervised anomaly detection. *IEEE Transactions on Neural Networks and Learning Systems*, PP, 1–14, <https://doi.org/10.1109/tnnls.2023.3344118>

Zou, Y., Jeong, J., Pemula, L., Zhang, D., Dabeer, O. (2022). Spot-the-difference self-supervised pre-training for anomaly detection and segmentation. (pp. 392–408). Springer, Cham.